International Journal of Heat and Mass Transfer 265 (2026) 128765

Contents lists available at ScienceDirect

International Journal of Heat and Mass Transfer

journal homepage: www.elsevier.com/locate/ijhmt

Comparative evaluation of dielectric liquids for single-phase immersion cooling of electronics

Shayan Aflatounian [a,1], Sarath Subramaniyan [a,1], Kai Luo [a,*], Sujan Dewanjee [a,b], Vishwanath Ganesan [a], Oliver R. Gittus [c], Erich A. Müller [c], Giles Prentice [d], Marc J. Payne [d], Andrew Stillwell [e], Paul V. Braun [a,b,f,g,h,i], Nenad Miljkovic [a,b,e,j,k,l,**]

[a] Department of Mechanical Science and Engineering, University of Illinois, Urbana, IL 61801, United States
[b] Materials Research Laboratory, University of Illinois, Urbana, IL 61801, United States
[c] Department of Chemical Engineering, Sargent Centre for Process Systems Engineering, Imperial College London, London SW7 2AZ, United Kingdom
[d] Advanced Fluids Research Castrol, bp technology Centre, Pangbourne RG8 7QR, United Kingdom
[e] Department of Electrical and Computer Engineering, University of Illinois, Urbana, IL 61801, United States
[f] Department of Materials Science and Engineering, University of Illinois, Urbana, IL 61801, United States
[g] Beckman Institute for Advanced Science and Technology, University of Illinois, Urbana, IL 61801, United States
[h] Department of Chemical and Biomolecular Engineering, University of Illinois, Urbana, IL 61801, United States
[i] Department of Chemistry, University of Illinois, Urbana, IL 61801, United States
[j] Institute for Sustainability, Energy, and Environment, Urbana, IL 61801, United States
[k] Air Conditioning and Refrigeration Center, Energy, and Environment, Urbana, IL 61801, United States
[l] International Institute for Carbon Neutral Energy Research (WPI-I2CNER), Kyushu University, 744 Moto-oka, Nishi-ku, Fukuoka 819–0395, Japan

ARTICLE INFO

Keywords:
Thermal management
Electronics
Single-phase immersion cooling
Dielectric liquids
Current leakage
Natural convection
Heat transfer
Device cooling
Data center
Server cooling

ABSTRACT

Rising heat fluxes in wide-bandgap power electronics and data center hardware have renewed interest in single-phase immersion cooling (SPIC) as a simple, scalable alternative to indirect liquid cooling as well as two-phase immersion cooling systems. However, the lack of standardized, property-based liquid coolant benchmarks has complicated engineering decisions. This study offers a comprehensive evaluation of the thermal and electrical performance of various dielectric liquids for SPIC of electronic devices. An analysis framework was developed using a figure of merit (FOM) based on natural convection correlations, allowing for property sensitivity and weight-factor assessments across different operating liquid temperatures. A buoyancy-driven SPIC experimental platform, featuring a commercial super junction (SJ) silicon MOSFET (drain tab size 10 mm × 12 mm), was built to measure the cooling and electrical insulation performance of 10 commercial dielectric liquids and 5 candidate chemistries not yet available commercially. Results reveal that high fluid thermal conductivity and density strongly improve cooling performance, while dynamic viscosity primarily limits it. Experimental data categorize the tested liquids into three tiers of cooling effectiveness: four commercial liquids in tier 3 with lowest junction-to-coolant thermal resistances of 7.0 – 7.8 K/W (3.27 – 3.75 (cm^2·K)/W), seven in tier 2 with thermal resistances of 5.9 - 6.4 K/W (2.82 – 3.08 (cm^2·K)/W), and four candidate liquids in tier 1 achieving the lowest resistances of 4.9 - 5.4 K/W (2.32 – 2.56 (cm^2·K)/W). Electrical insulation tests show most liquids maintain leakage currents below 5 nA at 550 V. These findings offer clear guidelines for dielectric liquid selection, supporting SPIC deployment in data centers, battery thermal management systems, and power electronics applications.

* Corresponding author.
** Corresponding author at: Department of Mechanical Science and Engineering, University of Illinois, Urbana, IL 61801, United States.
E-mail addresses: kailuo@illinois.edu (K. Luo), nmiljkov@illinois.edu (N. Miljkovic).
[1] Authors contributed equally to this work

https://doi.org/10.1016/j.ijheatmasstransfer.2026.128765
Received 20 January 2026; Received in revised form 28 February 2026; Accepted 25 March 2026
Available online 13 April 2026
0017-9310/© 2026 The Author(s). Published by Elsevier Ltd. This is an open access article under the CC BY-NC-ND license (http://creativecommons.org/licenses/by-nc-nd/4.0/).

Nomenclature

Latin symbols (alphabetical order)

A	Area [m^2].
a	Fitting coefficients [K/W].
b	Fitting coefficients.
c_p	Specific heat capacity [J/(kg·K)].
D	Drain.
DS	Driver Source.
E_B	Dielectric strength [kV/mm].
G	Gate.
g	Gravity [m/s^2].
h	Heat transfer coefficient [$W/(m^2 \cdot K)$].
h_{exp}	Estimated heat transfer coefficient [$W/(m^2 \cdot K)$].
I	Current [A].
I_{ds}	Drain-Source Current.
k	Thermal conductivity [W/(m·K)].
KD	Kelvin Drain.
KDS	Kelvin Driver Source.
KPS	Kelvin Power Source.
L	Characteristic length [m].
L_{gap}	Electrode spacing [mm].
Nu	Nusselt number.
p	Property of the fluid.
Pr	Prandtl number.
PS	Power Source.
Q	Device cooling power [W].
q'''	Volumetric heat generation [W/m^3].
Ra	Rayleigh number.
R_0	Shunt Resistance.
R_t	Thermal resistance [K/W].
T	Temperature [K].
t	Time [s].
T_c	Fluid characteristic temperature [K].
T_f	Fluid temperature [K].
T_{fp}	Flash point temperature [℃].
T_j	Device junction temperature [K].
T_s	Surface temperature [K].
u	Uncertainty.
V	Voltage [V].
Vol	Volume [m^3].
V_F	Forward Voltage.
V_{gs}	Transistor Gate Voltage.
w	Weight factor for property p_i.
w_{c_p}	Weight factor for specific heat capacity.
w_k	Weight factor for thermal conductivity.
w_β	Weight factor for volumetric thermal expansion coefficient.
w_μ	Weight factor for dynamic viscosity.
w_ρ	Weight factor for density.
x_0	Dependent physical property.

Greek symbols (alphabetical order)

β	Volumetric thermal expansion coefficient [1/K].
ΔT	Temperature difference between junction temperature and fluid temperature [K].
ε_r	Dielectric constant.
μ	Dynamic viscosity [mPa·s].
ρ	Density [kg/m^3].

Subscripts

B	Breakdown voltage.
c	Characteristic.
Cu	Copper drain tab.
ds	Drain-source (Device terminals).
f	Fluid.
F	Forward.
fp	Flash point.
gs	Gate-source (Device terminals).
i	Index for property.
j	Junction.
l	Leakage.
mfrc	Manufacturer calibration.
s	Surface.
Sh	Shunt.
t	Thermal.
TDAQ	Temperature measurement from Data Acquisition.

Abbreviations

2PIC	Two-phase Immersion Cooling.
AI	Artificial Intelligence.
API	American petroleum institute.
CHF	Critical Heat Flux.
DAQ	Data Acquisition.
DEHA	Bis(2-ethylhexyl) adipate.
DGDE	Diethylene glycol dibutyl ether.
DMM	Digital multimeter.
FOM	Figure of Merit.
GWP	Global Warming Potential.
HFE	Hydrofluoroether.
HPC	High-Performance Computing.
HTC	Heat Transfer Coefficient.
MO−12	Mineral oil (12.32 cSt at 40℃).
MO−24	High purity white mineral oil (24 cSt at 40℃).
MOSFET	Metal-Oxide-Semiconductor Field-Effect Transistor.
MS	Methyl salicylate.
PAO	Poly alpha olefin C20.
PCB	Printed Circuit Board.
PFAS	Per- and Polyfluoroalkyl Substances.
PFPE	Perfluorinated polyether.
PO	Paraffinic oil C15-C30.
PUE	Power usage effectiveness.
PVC	Polyvinyl Chloride.
SE	Synthetic ester.
SGF	Synthetic glycol-based fluid.
SIR	Surface Insulation Resistance.
SJ	Super junction.
SO−20	High purity silicon oil (20 cSt at 25℃).
SO−5	High purity silicon oil (5 cSt at 25℃).
SPHO	Synthetic paraffinic hydrocarbon oil C20-C24.
SPIC	Single-phase Immersion Cooling.
TC	Thermocouple.
TCB	1,2,4-Trichlorobenzene.
TD	Tetradecane.

1. Introduction

The past decade has witnessed a dramatic increase in the power density of electronic systems, driven by breakthroughs in computing and the growing scale of data infrastructure [1,2]. Advanced artificial intelligence (AI) workloads and high-performance computing (HPC) applications require processors and accelerators with ever-higher performance, which in turn generate more heat per unit area compared to earlier generations [3,4]. Analogous trends are observed in electric vehicles, where growing energy demands of power electronics and high-capacity battery systems pose challenges to thermal and electrical management [5,6]. Rising energy throughput, decentralized generation, and smarter grid demands impose complex thermal and dielectric stresses on high voltage transformers, prompting the development of advanced modeling and cooling strategies to improve reliability and efficiency [7,8].

Heat fluxes at the chip level have risen into the tens of Watts per square centimeter for current processors, with projections of future devices potentially exceeding 1 kW/cm^2 [9]. This steep upward trend in power density underscores a fundamental reality: removing heat has become as critical as computing itself in modern system design [10]. The consumption of computing infrastructure has surged, with global data centers already drawing approximately 415 TWh per year, accounting for 1.5% of the world's electricity [11]. In extreme cases, exascale supercomputers require 20–30 MW of power for efficient operation, with traditional cooling systems constituting up to 40% of the total electricity usage [12,13]. Increasing compute power density is pushing conventional thermal management techniques to their limits, as every Watt consumed ultimately becomes heat that must be dissipated, raising operational costs and threatening long-term system sustainability [14,15]. If heat is not efficiently removed, even brief operation at high loads can create local hotspots that drive junction temperatures beyond safe limits, degrading performance and decreasing device reliability [16]. Thus, maintaining safe temperatures amid steadily rising power dissipation now serves as a primary bottleneck for sustaining performance growth in electronics [17,18].

Air cooling, the main solution for decades, is increasingly inadequate in the face of these high power densities [19,20]. Traditional air-cooled heat sinks and fan systems rely on convection heat transfer to the surrounding air. However, the low thermal conductivity and heat capacity of air make it a poor coolant for high heat flux scenarios [21,22]. There is a practical upper limit to how much heat can be expelled by forced air, roughly around 30–45 kW per data center 42 U server rack [23]. Pushing further would require impractically large heat sink assemblies, very high airflow rates which would necessitate noisy, high-power fans and chilled air temperatures far below ambient. All of these approaches are unsustainable or inefficient. To cope with this thermal issue, attention has turned to liquid cooling technologies as a next-generation solution [24]. Compared to air, liquids have orders of magnitude higher volumetric heat capacity and greater thermal conductivity, allowing them to absorb and transport much more heat with a given flow [25]. By circulating a coolant in direct contact with hot components or their heat spreaders, liquid cooling can remove heat far more efficiently, enabling stable operation at heat loads that would overwhelm air cooling [26].

Over the years, liquid cooling methods have evolved in form and application. Early and modern studies on direct-to-chip liquid cooling have demonstrated that attaching cold plates or microchannel heat exchangers directly to processors significantly reduces thermal resistance by enabling efficient convective heat removal using water or water-glycol mixtures. Kandlikar and Hayner [27] established foundational thermal design principles for liquid-cooled cold plates, showing substantial improvements in heat removal capability compared to air cooling. Subsequent system-level investigations confirmed that cold plate cooling enables higher rack power densities while maintaining acceptable junction temperatures in computing hardware [28], whereas related applications in electrochemical and energy systems demonstrated similar advantages in managing localized heat generation through controlled liquid circulation [29]. Comprehensive reviews of single-phase and two-phase heat transfer enhancement techniques further quantified how microstructured channels and optimized flow architectures improve heat transfer coefficients and overall cooling effectiveness [30,31]. More recent developments employing advanced manufacturing approaches, including etched large footprint cold plates and additively manufactured fin architectures, have reported ultra-low thermal resistance and improved thermal-hydraulic performance suitable for next generation high power electronics [32–34]. Liquid cooling (through a cold plate) using water can achieve very low thermal resistance from chip to coolant, but it requires complex plumbing infrastructure and meticulous engineering safeguards since water is electrically conductive and can cause current leakage and shorting of electronics if a leak is present in the system [35].

An alternative approach is immersion cooling that fully submerges electronic components in an electrically non-conductive liquid, allowing the fluid to flow directly over and around all heat-dissipating surfaces for effective thermal management [36,37]. Because the liquid is in contact with components, heat is removed with minimal thermal resistance, and even irregularly shaped or densely packed assemblies can be cooled uniformly [38]. Reviews of immersion-cooled systems further report reductions in thermal resistance pathways because heat is transferred directly from component surfaces to the surrounding dielectric liquid rather than through intermediate interfaces [39]. Experimental demonstrations of water-based immersion cooling have further shown that direct liquid contact can sustain high heat flux operation while maintaining stable device temperatures, highlighting the potential performance ceiling achievable when electrical insulation challenges are addressed through protective packaging strategies [40]. In parallel, recent system-level investigations integrating data-driven and machine learning based control frameworks have illustrated how immersion cooling platforms can be dynamically optimized to improve thermal regulation and operational efficiency in electrified energy systems [41]. In addition, immersion cooling systems operate with minimal noise and no airborne dust since they eliminate high-speed fans and open-air circulation. This yields quieter operation, a cleaner environment for electronics, and potentially improved hardware longevity [42]. In addition, the heat absorbed by the liquid can be readily transferred to external heat exchangers for waste heat recovery, such as repurposing the heat for building heating, further enhancing the sustainability of this approach [43,44]. These benefits have led to a surge of interest in immersion cooling across various industries.

The two primary variants of immersion cooling technology, distinguished by how the coolant handles the heat, are single-phase and two-phase immersion cooling [45]. In single-phase immersion cooling (SPIC), a low dielectric constant (typically less than 2.5) coolant remains in the liquid state throughout the process with no phase change occurring [46]. As components heat up, the surrounding liquid warms but does not evaporate or boil [47]. The heated liquid is circulated by natural convection (buoyancy-driven SPIC) or is pumped within the immersion tank to further enhance single phase convection. The liquid is eventually pumped to an external heat exchanger where the heat is rejected to a secondary cooling loop (pump-driven SPIC) or outdoor air (dry or wet cooling), and the cooled liquid then returns to the immersion cooling tank [48]. Since no boiling occurs, the system design is relatively simple, and the liquid stays chemically stable over a wide operating range [49]. Single-phase immersion setups are straightforward to implement and generally use inexpensive dielectric liquids such as mineral oils [50]. However, their cooling performance is ultimately limited by the sensible heat capacity and other thermal properties of the liquid, which constrain how much heat can be carried away for a given flow rate [51].

Two-phase immersion cooling (2PIC), by contrast, relies on boiling of the coolant to dissipate heat. The dielectric fluid is selected to have a low boiling point typically ranging from 30°C to 75°C, so that heat from

the electronics causes the liquid to vaporize at the component surfaces [52]. This phase change absorbs a large amount of heat, effectively clamping component temperatures near the boiling point of the liquid [53,54]. The vapor then rises and condenses on a condenser integrated into the tank, releasing heat to a secondary loop. By leveraging latent heat, two-phase immersion achieves extremely high heat transfer coefficients and maintains very uniform component temperatures [55]. However, the dielectric fluids used in 2PIC require superior system sealing due to their high volatility and very low surface tension [56,57]. Beyond volatility, fluorinated two-phase liquids can act as aggressive solvents and plasticizers for common server and printed circuit board (PCB) materials like thermal greases, PVC wire insulation, and solder flux, leading to extractables that deposit on boiling sites, foul surfaces, and degrade long-term reliability [58]. Additionally, many low boiling point dielectric fluids have poor sustainability, high global warming potential (high-GWP), and high cost compared to SPIC fluids. Also, regulatory momentum around per- and polyfluoroalkyl substances (PFAS) is accelerating, as most commercially deployed 2PIC working fluids are fluorochemicals. Major suppliers of PFAS fluids (such as 3 M) are exiting the market, creating supply-chain and qualification risks [59,60]. In addition, there are no commercially adopted hydrocarbon dielectrics with suitably low boiling points and acceptable safety characteristics for 2PIC, whereas SPIC coolants are predominantly hydrocarbon liquids which avoid these PFAS issues [61]. Moreover, two-phase systems face dryout issues at the critical heat flux (CHF), posing a cooling risk under high power [62]. Thus, although 2PIC systems demonstrate strong potential, these limitations hinder their widespread adoption. In comparison, SPIC has gained greater commercial traction, particularly in data centers and cryptocurrency mining, where cost effectiveness and reliability outweigh the ultimate performance ceiling.

Despite the progress and promise of SPIC, one key open question is the choice of coolant. A wide variety of single phase dielectric liquid coolant options exist, ranging from mineral oils and synthetic hydrocarbon oils to natural esters and engineered fluorochemicals, each with distinct thermophysical and electrical properties [39,63]. These SPIC liquids differ in viscosity, thermal conductivity, specific heat capacity, dielectric strength, dielectric constant, and chemical stability among other factors. The role of liquid chemistry is also overlooked in determining how composition influences the physical properties, and how chemical aging affects the liquid performance [64,65]. Comparative data on different liquids under identical conditions are scarce because much of the existing literature documents immersion cooling results for only a single chosen liquid under different testing conditions. Additionally, the coolant must efficiently transfer heat while also remaining electrically inert and chemically compatible with the electronics. Equally important but often omitted in SPIC discussions is flammability. Flash point places a practical limit on thermal performance because liquids with lower viscosity and higher heat transfer potential typically exhibit lower flash points. This flammability performance trade-off provides important context for why certain chemistries are not widely adopted in practice, in addition to the electrical and material compatibility considerations. In practice, this balance involves trade-offs; thus, rigorous evaluation of both thermal performance and electrical compatibility for candidate liquids is critical [66,67], which, however, remains scarce in previous studies. Most studies focus solely on the thermal and flow behavior without considering electrical degradation, leakage current, or voltage stress effects [64,68]. Previous research largely relies on simplified setups that fail to capture the dynamic thermal-electrical interactions that occur under realistic workloads during immersion [68,69]. Furthermore, long-term stability and material compatibility remain critical yet underexplored. Prolonged exposure of electronics or other polymer compounds in certain dielectric liquids poses a risk of performance degradation and electronics malfunction [70,71]. These challenges highlight the need for a multidisciplinary approach to SPIC research that accounts for thermal, electrical, chemical, and reliability factors in tandem.

In this work, a systematic comparative analysis of single-phase immersion cooling is carried out using a comprehensive list of 15 dielectric liquids featuring a variety of different chemistry compositions, with the aim of quantifying how the choice of liquid influences both cooling effectiveness and electrical compatibility. Multiple liquids were compared in a controlled setup that integrated a real-world PCB-mounted SJ silicon MOSFET electronic device. The study investigated both the thermal and electrical performance of the dielectric liquids, illustrating how various liquid properties translate into real-world cooling outcomes and equipment reliability. The findings are intended to guide the selection of optimal dielectric liquids for future immersion-cooled systems, helping engineers balance thermal management requirements with electrical and material compatibility considerations.

2. Fundamental analysis on thermal performance

Since most electronic boards are placed vertically [40,61,66] in coolants in immersion cooling systems for easy access, the cooling performance is determined by the natural convection on vertical surfaces in a buoyancy-driven SPIC system. The heat transfer coefficient h, which is a measure of the rate at which heat is transferred per unit surface area per unit temperature difference between the solid device surface and the immersion liquid, can be expressed as:

$$h = \frac{k\mathrm{Nu}}{L}, \tag{1}$$

where Nu is the Nusselt number, k is the thermal conductivity of the liquid, and L is the characteristic length of the heat transfer surface. For a discrete device such as a Si chip, L is defined as the height (vertical dimension) of the plate in the direction parallel to the gravitational acceleration/growth of the boundary layer.

For natural convection on vertical surfaces, a well-established correlation for Nu is proposed by Churchill and Chu [72] for a constant heat flux boundary condition:

$$\mathrm{Nu} = \left[0.825 + \frac{0.387\mathrm{Ra}^{\frac{1}{6}}}{\left(1 + \left(\frac{0.437}{\mathrm{Pr}}\right)^{\frac{9}{16}}\right)^{\frac{8}{27}}}\right]^2, \qquad \mathrm{Ra} < 10^{12} \tag{2}$$

where Pr is the liquid Prandtl number, and Ra is the liquid Rayleigh number, which describes the impact of thermal transport via diffusion compared to convection in a buoyancy-driven flow, given by:

$$\mathrm{Ra} = \frac{g\beta(T_s - T_f)\rho^2 c_p L^3}{\mu k}, \tag{3}$$

where g is gravitational acceleration, β is the thermal expansion coefficient of the immersion liquid, T_s is the surface temperature, T_f is the far-field liquid temperature of the immersion liquid, μ is the liquid dynamic viscosity of the immersion liquid, ρ is the liquid density of the immersion liquid, and c_p is the liquid specific heat capacity of the immersion liquid.

Combining Eqs. (1)–(3), the immersion cooling heat transfer coefficient can be expressed as:

$$h = \frac{k}{L}\left[0.825 + \frac{0.387\mathrm{Ra}^{1/6}}{\left(1 + (0.437/\mathrm{Pr})^{9/16}\right)^{8/27}}\right]^2. \tag{4}$$

While Eq. (4) describes the heat transfer coefficient for a specific geometry and operating condition, direct comparison between different immersion coolants using this expression is not straightforward because the heat transfer coefficient depends on system dimensions and temperature differences in addition to fluid properties. To enable a generalized comparison between candidate dielectric liquids, a figure of merit

(FOM) is introduced by removing constants, geometric parameters, and temperature-dependent terms from the heat transfer coefficient. This approach isolates the contribution of intrinsic thermophysical properties to buoyancy-driven heat transfer performance and allows fluid selection to be evaluated independent of a particular device configuration. Based on the heat transfer coefficient, the figure of merit (FOM) is defined by removing constants, geometry, and temperatures as the following:

$$\mathrm{FOM} = \frac{k\left(\frac{\beta c_p \rho^2}{\mu k}\right)^{1/3}}{\left(1+\left(\frac{k}{c_p \mu}\right)^{9/16}\right)^{16/27}} \quad . \tag{5}$$

The FOM shows that the immersion cooling performance in a buoyancy-driven SPIC system is determined by the five physical properties of the liquid coolant, namely its density ρ, dynamic viscosity μ, specific heat capacity c_p, thermal conductivity k, and thermal expansion coefficient β. By expressing performance solely in terms of fluid properties, the FOM provides a physics-based framework for comparing different dielectric fluids tested in this study and for interpreting experimentally observed cooling trends in relation to fundamental transport mechanisms. This formulation yields a non-dimensional value based on SI units, and is consistent with previously reported convection-based FOM analyses used for coolant evaluation and fluid screening in the literature [73–75].

A sensitivity analysis based on FOM is carried out to examine how the change in the independent property of a liquid immersion coolants impacts the FOM under given assumptions, therefore determining the driving factors of the cooling performance. The variance of the FOM due to a property change can be calculated by,

$$\frac{\Delta FOM}{FOM}\Big|_{x_0} = \frac{FOM(x_0+\Delta x) - FOM(x_0)}{FOM(x_0)}, \tag{6}$$

where x refers to one dependent physical property.

A commonly used single-phase heat transfer fluid, MO−24, a high-purity white mineral oil (24 cSt at 40°C), is used as an example for sensitivity analysis, and the results are given in Fig. 1. The temperature reference for thermal properties is set as 60°C, and each property was independently varied while the remaining properties were held constant. The sensitivity sweep separates the liquid properties into three groups. Thermal conductivity and density have the strongest positive impact. Doubling either increases the FOM by approximately 60%,

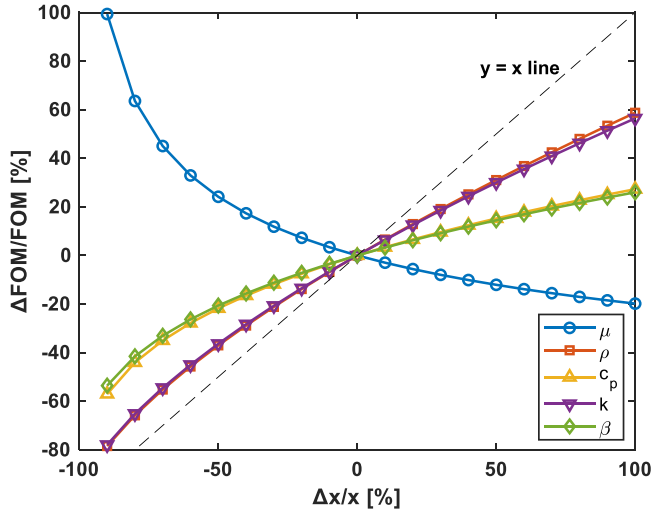


Fig. 1. Sensitivity analysis for mineral oil MO−24. The temperature reference for thermal properties is set as 60°C in the analysis. Data points represent calculations with lines between data points representing guiding lines only.

while halving reduces it by approximately 40%. Their overlap highlights that conductivity and buoyancy contribute equally to increasing the Rayleigh number. Thermal expansion coefficient and specific heat capacity form a moderate tier. Doubling either increases the FOM by approximately 25%, and halving reduces the FOM by 20%. Their influence comes mainly from buoyancy and thermal storage. Dynamic viscosity acts oppositely. Doubling the dynamic viscosity cuts the FOM by 20%, whereas reducing it by 90% nearly doubles the performance. Overall, the analysis indicates that optimal immersion coolants should combine high liquid thermal conductivity, liquid density, liquid expansion coefficient and liquid heat capacity, while minimizing liquid dynamic viscosity.

Note that each property may have a different range of changes when comparing different liquids. For example, dynamic viscosity between different fluids could vary in the 1–2 orders of magnitude at the same temperature, while the thermal conductivity difference between most dielectric fluids only varies between 1–2-fold. Moreover, each property also exhibits different dependence on temperature for different fluids. To further evaluate the impact of physical properties on the immersion cooling performance, a weight-factor framework is used with consideration of temperature dependence. Based on Eq. (5), the partial derivative of FOM can be expressed as [76]:

$$\begin{aligned} \partial FOM = &\left(\frac{\partial FOM}{\partial \mu}\frac{\partial \mu}{\partial T}\right)\Big|_{\mu}\partial T + \left(\frac{\partial FOM}{\partial \rho}\frac{\partial \rho}{\partial T}\right)\Big|_{\rho}\partial T + \left(\frac{\partial FOM}{\partial c_p}\frac{\partial c_p}{\partial T}\right)\Big|_{c_p}\partial T \\ &+ \left(\frac{\partial FOM}{\partial k}\frac{\partial k}{\partial T}\right)\Big|_{k}\partial T + \left(\frac{\partial FOM}{\partial \beta}\frac{\partial \beta}{\partial T}\right)\Big|_{\beta}\partial T, \end{aligned} \tag{7}$$

$$w_x = \left(\frac{\partial FOM}{\partial x}\cdot\frac{\partial x}{\partial T}\right)\Big|_{x}, \tag{8}$$

where w_x is defined as the weight factor for the property, x. The first derivative characterizes the impact of physical property on heat transfer, while the second derivative quantifies the temperature dependence of that property.

Another commonly used dielectric fluid, HFE−7700, with distinctly different physical properties, is used to compare with MO−24. Chemically, mineral oils like MO−24 are a complex mixture of various hydrocarbon compounds derived from petroleum, while HFE fluids are fluorinated organic compounds. Due to the uniquely different molecular structures, mineral oils generally have high thermal conductivity, making them suitable candidates for heat transfer fluids. However, they exhibit higher viscosity than HFE fluids, limiting their performance in immersion cooling systems. Fig. 2 is presented as an illustrative comparison between the two representative dielectric fluid classes to demonstrate how temperature-dependent thermophysical properties influence the weight-factor framework introduced in Eqs. (7, 8). These fluids are not used to establish the general conclusions of this study but rather to provide physically representative examples for interpreting the analytical framework prior to applying it to the broader set of dielectric fluids investigated experimentally. Fig. 2 shows the comparison of physical properties between MO−24 and HFE−7700 with temperatures ranging from 0 to 150°C. The thermal expansion coefficients, which are often not provided by the manufacturers, are estimated based on temperature-dependent density data as below,

$$\beta = -\frac{1}{\rho}\left(\frac{\partial \rho}{\partial T}\right)_P, \tag{9}$$

where the subscript P indicates that the pressure is constant during the expansion.

Fig. 3 shows how each physical property governs the FOM at different temperatures for MO−24 and HFE−7700. The figure shows that viscosity dominates the FOM at low temperatures for both fluids, about 70–80% at 0°C, but its influence declines with temperature as the contribution is reallocated to the other properties. For MO−24, W_μ drops from 70% to 30% by 150°C, while the shares of W_{c_p} and W_ρ grow

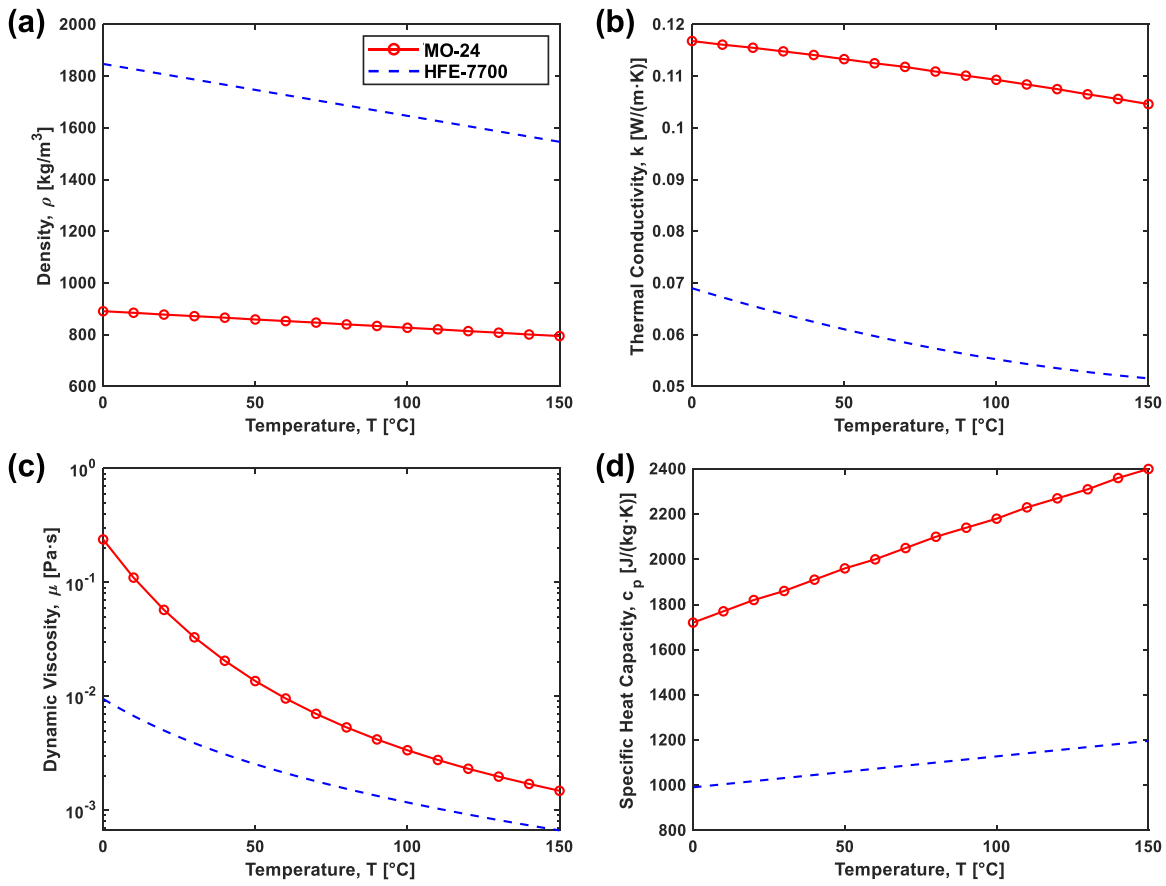


Fig. 2. Physical property comparison between MO−24 (red circles) and HFE−7700 (blue dashed line) showing: (a) liquid density, (b) liquid thermal conductivity, (c) liquid dynamic viscosity (logarithmic scale), and (d) liquid specific heat capacity, as functions of fluid temperature (T_f). The legend in (a) is applicable to (b), (c), and (d).

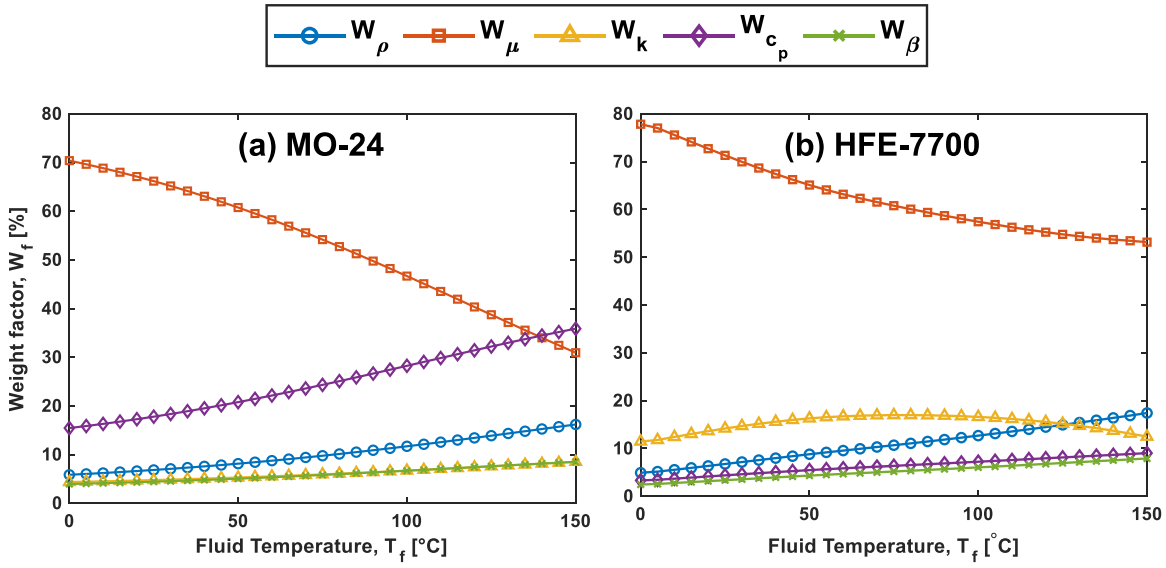


Fig. 3. Weight factor change as a function of liquid temperature (T_f) for different physical properties for (a) MO−24, and (b) HFE−7700. The y-axis of (b) is the same as the y-axis of (a).

steadily. W_{c_p} becomes co-dominant with viscosity above 140°C and is the largest term by 150°C liquid temperature. Liquid density rises from a few percent to 10–20%, W_β increases gradually but remains secondary, and W_k changes only modestly. For HFE−7700, the fall in W_μ is gentler and it stays as the leading contributor across the entire range of liquid temperatures. W_k shows a mild mid-temperature peak, and W_ρ, W_{c_p}, and W_β all gain with temperature but remain below W_μ. Overall, regardless of the liquid, W_μ shows a dominant impact on the weight factor due to its high dependence on temperature, while the impacts of W_k, W_ρ, W_{c_p}, and W_β remain relatively low (less than 20%). Put differently, the temperature-driven redistribution is stronger in MO−24, where W_{c_p} and W_ρ take over a larger share as W_μ weakens.

3. Experimental apparatus

3.1. Immersion cooling setup

Fig. 4 shows a schematic of the buoyancy-driven SPIC experimental setup. It consists of a 6-inch cubic glass tank (Marina Cubus Glass Betta Kit, Rolf C. Hagen Inc.) with 80% volume filled with the test dielectric liquid. A custom designed PCB with a mounted electronic device was vertically immersed in the fluid under test. Specifics of the PCB and device are discussed in the next section. A 3D-printed holder is used to install the board in the center of the tank to ensure consistent positioning. The distance between the device and the fluid level is approximately 6 cm. When the electronic device is powered, the heat generated from the device dissipates into the dielectric fluid through natural convection. To ensure consistent conditions across different fluids, the fluid bath temperature was maintained at around room temperature (20°C) using a stainless-steel coiled heat exchanger (lab-made coil from 0.25in stainless tube) surrounding the PCB. The coil is connected to a cooling loop driven by a circulating pump (Type RS 15–6, ZeroPone) and a chiller (LM61GX1A110C LM6 Benchtop Chiller, PolyScience). Two T-type thermocouples (Thermocouple Beaded Wire Sensor Type T 40 Gage, Evolution Sensors and Controls, LLC), read by the NI−9213 module, were placed at different positions within the bath away from the device to monitor bath temperature. The device power and junction temperature measurements were recorded using the NI−9229 module, with data acquisition and control implemented through a LabVIEW interface with a sampling rate of 2 Hz.

3.2. Electronic device

An SJ silicon MOSFET power device (Infineon, IPDQ60T017S7) is used in this study as the heating source for evaluating immersion cooling performance, as well as the electronic component for evaluating electrical insulation performance [77]. This device features a transistor suitable for low frequency switching and high-pulse current applications such as solid relays and line rectification. The package has a top-cooled design with a cooling surface (drain tab) of about 10 mm × 12 mm, ideal for testing immersion cooling of electronics. Most importantly, the device features an embedded temperature sensor for accurate junction temperature measurement, which is critical for thermal performance characterization. Previous immersion cooling studies using electronic devices struggled with accurate junction temperature measurement as they relied on unreliable surface-mounted temperature sensors or time-consuming calibration of device resistance [78–80].

The Infineon device is shown in Fig. 5(a). The device was soldered onto a custom-designed laminate PCB as shown in Fig. 5(b, c). The PCB employs traces for gate control (G and DS), drain (D), and power source (PS) for connecting corresponding pins of the device. Kelvin connections (KPS, KD, and KDS) were also implemented for direct voltage readings to prevent the voltage drops across the traces. The T connection was used for measuring the forward voltage (V_F) across the integrated temperature sensor, which exhibits a linear relation to the junction temperature and was calibrated before tests. During the experiment, the transistor gate voltage (V_{gs}) was set as a constant at 5 V while the drain-source current (I_{ds}) increased step by step, resulting in an increasing power operation of the device. The experiment was halted when the device junction temperature reached 140 °C, maintaining a safe margin below the manufacturer rated limit of 150°C [77].

3.3. Dielectric fluids

A total of 10 commercial dielectric fluids were selected for testing in this study. This comprehensive list includes commonly used fluids in immersion cooling, such as silicon oils, fossil derived synthetic hydrocarbons such as polyalphaolefins (PAOs), ester-based oils, and fluorinated fluids. A well-established approach to defining hydrocarbon fluids in this area is by using the API classification system, which classifies base stocks via their production, composition and viscometric performance [81]. Group I to III are refined from crude oil whereas group IV are fully synthetic produced fluids such as PAOs; group V contains anything that does not fall into groups I-IV. We have used this approach to describe where the fluids tested fall into this classification. Generally, hydrocarbons fluids which fall into groups I to IV are complex mixtures of compounds and not a discrete molecular structure. In addition, 5 potential organic fluid candidates were also tested to explore the potential of organic fluids with different distinct molecular structures, including tetradecane, bis(2-ethylhexyl) adipate, diethylene glycol dibutyl ether, 1,2,4-trichlorobenzene, and methyl salicylate. The selected list represents a diverse range of dielectric liquids with different chemistries (hydrocarbons, ester-based, silicone-based, fluorinated fluids), as well as other commercially unavailable organic compounds with thermophysical properties that suggest high performance in immersion cooling. The set of dielectrics tested includes both commercially deployed liquids for benchmarking the current practice, and candidate chemistries with distinct molecular structures for exploring performance limits and formulation opportunities. Table 1 shows a summary of the thermophysical properties of the tested fluids measured at 25°C.

4. Measurement and data reduction

4.1. Junction temperature measurement

The Infineon device employs an integrated on-chip temperature sensor based on the forward voltage characteristics of a series of three diodes. Located close to the active cells of the semiconductor die, the sensor provides reliable junction temperature readings and faster response during transient tests compared to conventional techniques. The relation between forward voltage (V_F) across the temperature

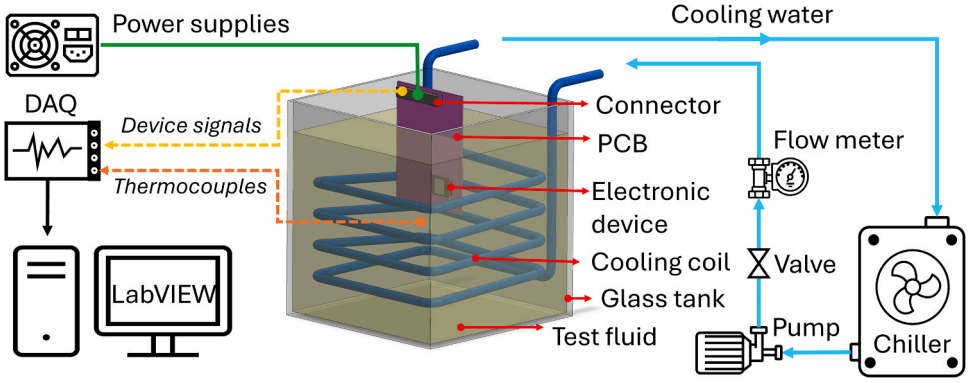


Fig. 4. Not-to-scale schematic of the experimental setup showing the immersion tank with the stainless-steel coiled heat exchanger inserted for temperature control.

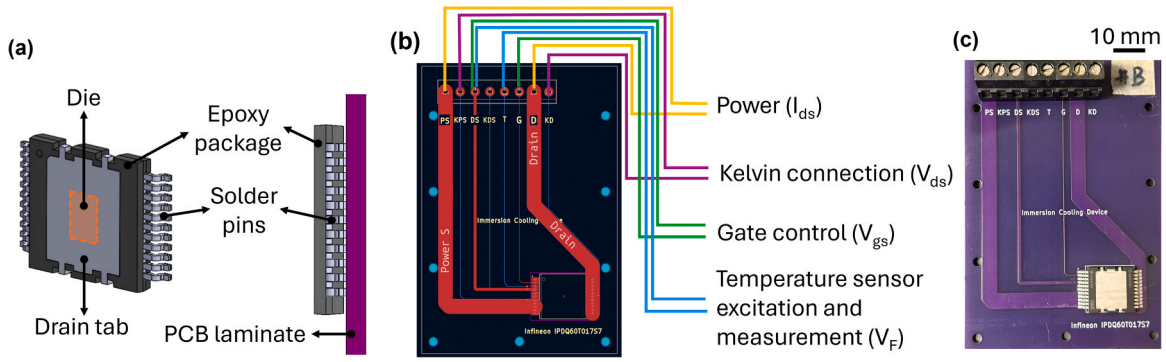


Fig. 5. (a) Schematic of the Infineon device package used for powering and heating. (b) CAD image of the custom PCB designed to heat up the device with the trace layouts labeled. (c) Photograph of the PCB with the soldered Infineon device on it in the bottom right corner.

Table 1
Thermophysical properties of tested dielectric fluids at 25°C. Values reported at indicated temperature when 25°C data is unavailable.

Fluid Name	API definition	Chemistry	Symbol	ρ [kg/m^3]	μ [mPa·s]	c_p [J/(kg·K)]	k [W/(m·K)]	β [1/K]	T_{fp} [°C]	ε_r	E_B [kV/mm]
High purity silicon oil (20cSt at 25°C)	Group V	Polydimethylsiloxane	SO-20	950	19	1600[a]	0.145[a]	1.07e-03[a]	232	2.68	15
High purity silicon oil (5cSt at 25°C)	Group V	Polydimethylsiloxane	SO-5	910	4.55	1600[a]	0.117[a]	9.60e-04[a]	135	2.59	15
Poly alpha olefin C20	Group IV	Poly alpha olefin	PAO	792	6.1	2035	0.138	8.50e-04	152	2.1[a]	20
Paraffinic oil C15-C30	Group III	Synthetic paraffinic hydrocarbon oil	PO	828	12.1	1850	0.131	8.70e-04	162	2.1[a]	14
Mineral oil (12.32cSt at 40 °C)	Group I	Technical grade white mineral oil	MO-12	822	10.2[a] at 40°C	2000[a]	0.113[a]	9.00e-04[a]	198	2.2[a]	20[a]
Synthetic paraffinic hydrocarbon oil C20-C24	Group IV	Mixed feed Poly alpha olefin	SPHO	820	5.9[a] at 40°C	2212.1 at 40°C	0.137 at 40°C	6.70e-04	203	2.1	24
Synthetic ester	Group V	Synthetic ester-based oil	SE	910	7.007[a] at 40°C	1970	0.148	2.00e-04[a]	203	3.9[a]	32
Perfluorinated polyether	Group V	Perfluorinated Polyether	PFPE	1790	4.3	965	0.065	1.10e-03	N/A	1.94	16
High purity white mineral oil (24cSt at 40°C)	Group I	High-purity white mineral oil	MO-24	875	20.5 at 40°C	1840	0.115	8.92e-04 at 200°C	199	2.14	15[a]
Synthetic glycol-based fluid	Group V	Polyalkylene glycol-based thermal fluid	SGF	920 at 40°C	38.8 at 40°C	1976 at 40°C	0.181 at 40°C	3.43e-04	248	2.5[a]	16[a]
Tetradecane	Group V	Straight-chain alkane hydrocarbon	TD	762	2.14	2209	0.138	2.40e-03	110	2.03	16[a]
Bis(2-ethylhexyl) adipate	Group V	Diester of 2-ethylhexanol and adipic acid	DEHA	925	13.7	2066.9	0.143	2.50e-03	196	3.9	16[a]
Diethylene glycol dibutyl ether	Group V	Glycol ether	DGDE	885	2.97	2100	0.146	2.16e-03	118	2.53	15[a]
1,2,4-Trichlorobenzene	Group V	Halogenated aromatic	TCB	1450	1.85	1062	0.112	1.95e-03	105	3.99	15[a]
Methyl salicylate	Group V	Methyl ester of Salicylic acid	MS	1174	2.56	1626	0.144	2.00e-03	96	9.47	15[a]

[a] Estimated value based on similar fluids if the data is not provided by the manufacturer.

sensor and junction temperature (T_j) was calibrated in the temperature-controlled oven. A constant bias current of 200 μA was applied to the sensor using a combination of an Agilent 6623A DC power supply set to 8 V and current source module REF200 (Texas Instruments [82]). A T-type thermocouple placed close to the device was used for reference temperature measurement. Fig. 6 shows the calibration curve of two different devices (1 and 2). For each test, the temperature inside the oven was changed step by step, allowing the voltage reading and reference temperature to stabilize to ensure a thermal equilibrium. The device was also powered off during calibration to avoid self-heating. The combined dataset was used to fit a linear correlation between T_j and V_F, expressed by:

$$T_j = 410.576 - 195.88V_F \quad . \tag{10}$$

Fig. 6 showed that the data of boards 1 and 2 overlapped, and the fitting correlation showed an R-square value of 0.9999, indicating the excellent stability of the temperature sensing.

4.2. Thermal performance

During the thermal performance test, the source-drain current I_{ds} was controlled by a variable DC power supply (ATO-JK3060K) to incrementally raise the device temperature in steps of approximately 10°C. After each current step, steady state was determined when the junction temperature stabilized to within a minimum standard deviation (< 0.1° C). After each cycle, the PCB was removed and cleaned using acetone and compressed air to remove any residual fluid. The same cleaning procedure was applied to the stainless-steel coil before switching to the next fluid to avoid contamination. Each dielectric fluid was tested under identical conditions. The device cooling power (Q) is calculated by:

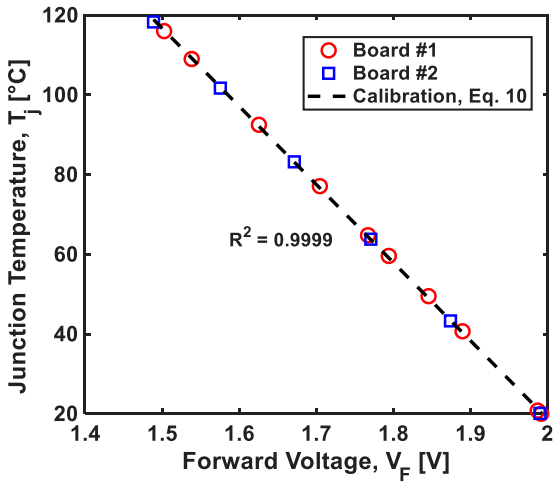


Fig. 6. Device temperature calibration data from two independent board device combinations with a linear fit (dotted line) representing the user-defined calibration curve (see Eq. 10).

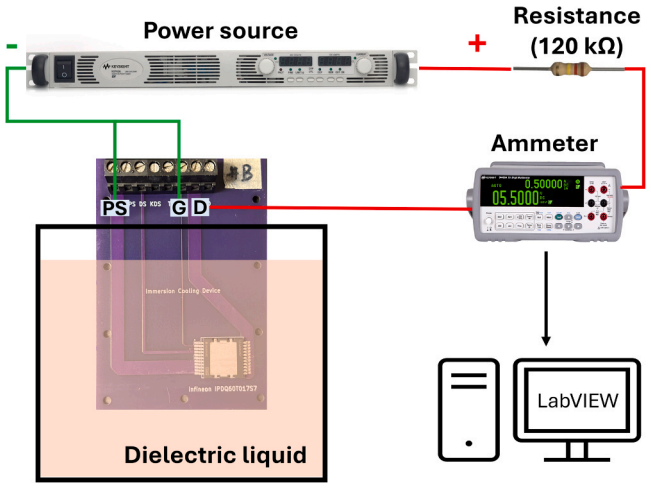


Fig. 7. Schematic of the current leakage test diagram. Schematic not to scale.

$$Q = I_{ds} V_{ds} \quad , \tag{11}$$

where V_{ds} is the source-drain voltage measured through Kelvin connections, and I_{ds} is measured by measuring the voltage (V_0) across a shunt resistance with a known value ($R_0 = 2m\Omega$):

$$I_{ds} = \frac{V_0}{R_0} \quad . \tag{12}$$

The fluid bath temperature (T_f) is estimated by averaging the temperatures from two thermocouples as:

$$T_f = \frac{T_{f,1} + T_{f,2}}{2} \quad . \tag{13}$$

The characteristic temperature (T_c) of sometimes called the film temperature of the fluid is calculated as:

$$T_c = \frac{T_f + T_j}{2} \quad . \tag{14}$$

The overall thermal resistance (R_t) for immersion cooling is expressed as:

$$R_t = \frac{T_j - T_f}{Q} \tag{15}$$

Uncertainty in measured parameters was accounted for by using standard statistical methods during post-processing. Experimental fluid properties were evaluated with junction temperature (T_j) ranging from 20 to 140 °C and fluid bulk temperature of $T_f = 20$ °C.

4.3. Current leakage

The current leakage procedure measures the leakage current through the Infineon device while immersed in the various dielectric liquids. The test uses the same Infineon device with the transistor in the OFF state. In the OFF-state configuration, the gate and source terminals of the transistor are shorted ($V_{gs} = 0$ V). These shorted terminals are connected in series with the digital multimeter (DMM), a power supply, and a current-limiting resistor (120 kΩ) as shown in Fig. 7. The negative terminal of the power supply is connected to the gate/source, and the positive terminal is connected to the drain. This ensures the transistor is biased in the OFF state, where any significant leakage current indicates failure or poor insulation. In real applications, this OFF configuration describes the leakage current through a transistor switch when it is not supposed to conduct (nanoampere range). If there is ineffective insulation or if the package has defects, higher currents may flow through the dielectric fluids rather than remaining negligible. Additionally, because the voltage is applied across terminals of the same device, the distance the leakage current must travel through the dielectric liquid is relatively small; in this case, 17 mm.

This configuration is derived from standard Surface Insulation Resistance (SIR) tests used in industry to detect short circuits in tightly spaced conductor traces [83–85]. The current leakage test was conducted immediately after thermal testing to assess dielectric insulation and fluid compatibility under electrical stress [66]. Test voltages of 100 V, 300 V, and 550 V were applied sequentially, and current data were recorded at 1 Hz using the LabVIEW interface through Keysight 34465. A digital multimeter transient current was recorded for 3 min after the voltage was applied. The average steady state leakage current was then calculated. Transient data was also plotted to compare the steady state leakage current and stabilization time across fluids.

4.4. Uncertainty analysis

The instrument specifications to measure the temperature and voltage drop associated with the device, shunt resistance, and the temperature sensor diode were directly adopted as the uncertainty limits for all the input parameters. The individual contributions for each of the parameters were combined through the Root Sum Squared (RSS) method. The adopted limits for each of the measured input parameters are shown in Table 2.

The uncertainty in average fluid temperature (u_{T_f}) is written as an RSS of the thermocouple sensor uncertainty (u_{TC}) and the NI−9213 DAQ measurement uncertainty (u_{TDAQ}), expressed by:

Table 2
Adopted uncertainty limits for input parameters.

Quantity	Uncertainty symbol	Uncertainty
NI−9213 Temperature reading, T_{DAQ}[°C]	u_{TDAQ}	$\pm(0.03\%*T_{DAQ} + 0.8)$ [°C]
Thermocouple sensor, TC [°C]	u_{TC}	±0.5 [°C]
NI−9229 – Forward diode voltage, V_F[V]	u_{V_F}	$\pm(0.03\%*V_F + 0.0008)$ [V]
NI−9229 – Drain-source voltage, V_{ds}[V]	$u_{V_{ds}}$	$\pm(0.03\%*V_{ds} + 0.0008)$ [V]
NI−9229 – Shunt voltage, V_{Sh}[V]	$u_{V_{Sh}}$	$\pm(0.03\%*V_{Sh} + 0.0008)$ [V]
Leakage current, I_l[A]	u_{I_l}	$\pm(0.005\%*I_l + 50pA)$ [A]
Shunt resistance, R_{Sh}[Ω]	$u_{R_{Sh}}$	±0.0025 [Ω]

$$u_{T_f} = \sqrt{(u_{TC})^2 + (u_{TDAQ})^2} \quad . \tag{16}$$

The uncertainty in the junction temperature (u_{T_j}) is inferred from the first order propagation associated with the forward bias voltage relation from Eq. (10) and can be expressed by Eq. (17). For the characteristic fluid temperature expressed in Eq. (14), the first order propagated uncertainty (u_{T_c}) associated is shown in Eq. (18). The reported final uncertainty in temperature difference between the junction and fluid temperature ($u_{\Delta T}$) is expressed as an RSS of uncertainty associated with both junction and average fluid temperature as expressed by Eq. (19) from Eq. (10).

$$u_{T_j} = \left|\frac{\partial T_j}{\partial V_F}\right| u_{V_F} \quad , \tag{17}$$

$$u_{T_c} = \frac{1}{2}\sqrt{\left(u_{T_j}\right)^2 + \left(u_{T_f}\right)^2} \quad . \tag{18}$$

$$u_{\Delta T} = \sqrt{(u_{TC})^2 + (u_{NI-9213})^2} \quad . \tag{19}$$

The shunt resistance used to measure the current through the drain-source, is expressed by Eq. (20) in terms of voltage drop across the shunt and shunt resistance. Eq. (21) expresses the sensitivity terms associated with the uncertainty propagation through the associated variables. Eq. (22) shows the final uncertainty associated with the drain-source current.

$$I_{ds} = \frac{V_{Sh}}{R_{Sh}} \quad , \tag{20}$$

$$\frac{\partial I_{ds}}{\partial V_{Sh}} = \frac{1}{R_{Sh}} \quad ; \quad \frac{\partial I_{ds}}{\partial R_{Sh}} = \frac{-V_{Sh}}{R_{Sh}^2} = -\frac{I_{ds}}{R_{sh}} \quad , \tag{21}$$

$$u_{I_{ds}} = \sqrt{\left(\frac{\partial I_{ds}}{\partial V_{Sh}} u_{V_{Sh}}\right)^2 + \left(\frac{\partial I_{ds}}{\partial R_{Sh}} u_{R_{Sh}}\right)^2} = \sqrt{\left(\frac{u_{V_{Sh}}}{R_{Sh}}\right)^2 + \left(-\frac{I_{ds}}{R_{sh}} u_{R_{Sh}}\right)^2} \quad . \tag{22}$$

Similarly, for Eq. (11) and the associated device cooling power, the sensitivity terms for uncertainty propagation are given by Eq. (23). The ultimate propagated uncertainty for the device cooling power (u_Q) is expressed by Eq. (24). For overall thermal resistance (R_t) expressed by Eq. (15), its uncertainty (u_{R_t}) is given by Eq. (25) where the uncertainty in power (u_Q) is one of the dominant contributors.

$$\frac{\partial Q}{\partial I_{ds}} = V_{ds} \quad ; \quad \frac{\partial Q}{\partial V_{ds}} = I_{ds} \tag{23}$$

$$u_Q = \sqrt{\left(\frac{\partial Q}{\partial I_{ds}} u_{I_{ds}}\right)^2 + \left(\frac{\partial Q}{\partial V_{ds}} u_{V_{ds}}\right)^2} = \sqrt{\left(V_{ds} u_{I_{ds}}\right)^2 + \left(I_{ds} u_{V_{ds}}\right)^2} \tag{24}$$

$$u_{R_t} = \sqrt{\left(\frac{u_{\Delta T}}{Q}\right)^2 + \left(\frac{\Delta T}{Q^2} u_Q\right)^2} \tag{25}$$

Limit values from Table 2 were used to compute the final average uncertainty associated with all data points for the tested fluids, as summarized in Table 3.

Table 3
Average uncertainties associated with reported quantities for thermal analysis.

Quantity	Average uncertainty
Heating power, Q[W]	±0.29 [W]
Temperature difference, ΔT[K]	±0.98 [K]
Fluid Characteristic temperature, T_c[K]	±0.49 [K]
Leakage current, I_l[A]	±50 [pA]
Thermal resistance, R_t[K/W]	±0.41 [K/W]

5. Results and discussion

Fig. 8 compares the steady state junction-to-bath temperature rise ($\Delta T = T_j - T_f$) of the Infineon device as a function of electrical power input (Q) for all 15 dielectric fluids. The slope of each trace is the effective thermal resistance according to Eq. (15) and provides a direct metric of cooling efficacy which will be discussed later. According to the figure, three performance tiers emerge. Tier 1 includes MS, DGDE, TD, and TCB (see Table 1 for fluids), which exhibit the flattest slopes, holding ΔT below 120°C even as power approaches 25 W, which translates to $R_t \approx 5$ K/W (Eq. 15). These liquids pair low dynamic viscosity with comparatively high thermal conductivity, enhancing the Rayleigh number and convective heat transfer coefficient as predicted by the FOM analysis in **Section II**. Tier 2, which consists of SO−5, PAO, PO, SPHO, SE, DEHA, and PFPE clusters around $R_t \approx 6$ K/W, while tier 3 includes SO−20, MO−12, MO−24, and SGF, showing the steepest slopes ($R_t > 7$ K/W). The experimental hierarchy, therefore, aligns with the weight-factor rankings, where the best coolants are those that simultaneously maximize liquid thermal conductivity (k) and density (ρ) while minimizing dynamic viscosity (μ).

Fig. 9 shows the overall thermal resistance R_t (Eq. 15) as a function of the characteristic fluid temperature, T_c. The 3 tiers identified are clearer and separate in order. Two key trends appear. First, every fluid shows a decline in R_t with higher liquid temperature of approximately 20–30% from 20°C to 60°C. This is because dynamic viscosity decays exponentially with temperature, while thermal conductivity (k) and expansion coefficient (β) change far less. This confirms that viscosity is the dominant antagonist identified in the sensitivity sweep. Second, the ordering of the fluids remains largely invariant with temperature, indicating that the relative differences in the thermophysical properties between fluids outweigh their variation over the operational temperature window (Eq. 5). For example, silicon oil 20 cSt never overtakes silicon oil 5 cSt. Among commercial products in the study which form tiers 2 and 3, selecting a top-tier commercial coolant (Tier 2, 6 K/W) over a lower-tier commercial option (Tier 3, 7 - 8 K/W) lowers thermal resistance by around 17–33%, underscoring the importance of optimal coolant choice at the system level. Notably, all Tier 1 fluids are candidate chemistries, where their 5 K/W performance represents a 15–20% improvement against the commercial products in tier 2, indicating headroom for new formulations via compositional tuning. Fig. 9 demonstrates that selecting an intrinsically low viscosity fluid is more influential than relying on thermal thinning during operation, a practical guideline for data center design where inlet temperatures are constrained by reliability considerations. However, in pumped SPIC, the heat transfer coefficient scales with fluid thermal conductivity ($h = Nu \cdot k/L$); thus, coolants with high thermal conductivity are expected to outperform even the top-tier commercial products under forced flow conditions.

Physically, the total thermal resistance between the junction and fluid comprises conduction through the package and convection into the dielectric fluid. The thin, highly conductive drain tab offers a shorter conduction path thereby making package resistance negligible compared to fluid-side resistance. The convective heat transfer performance for the dielectric fluids was then quantified through the corresponding natural convection heat transfer coefficient. In practice, estimation of the actual wetted area is nontrivial since the device geometry involves multiple irregular 3D surfaces. Therefore, the vertical drain copper tab as shown in Fig. 5(a) with a well-defined geometry was selected as the reference surface for evaluating heat transfer coefficient. The fraction of total heat dissipated through the drain tab was estimated through steady-state thermal simulation in ANSYS, which were validated against the experimentally measured junction-to-fluid temperature against device power input curves for 3 representative fluids each selected from a different performance tier. The validation ensured heat flow portioning accurately captured physical system behavior. The experimental net heat dissipated through the drain tab, Q_{Cu}, was estimated to be around 26% of the total heating power, Q, over the

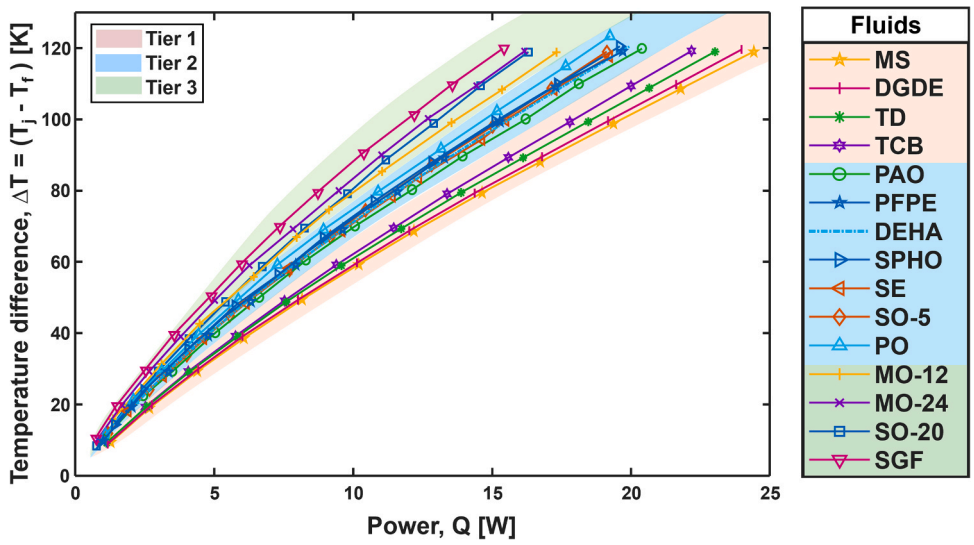


Fig. 8. Thermal performance of the different dielectric liquids tested under steady state conditions. The results show the measured junction-to-fluid temperature difference ($\Delta T = T_j - T_f$) as a function of the device power input (Q). Uncertainty in the measured temperature difference and input power are smaller than the symbol sizes and are not shown for clarity. Lines connecting the data points are guiding lines only, and do not represent any statistical fit. See Table 1 for fluid symbol definition.

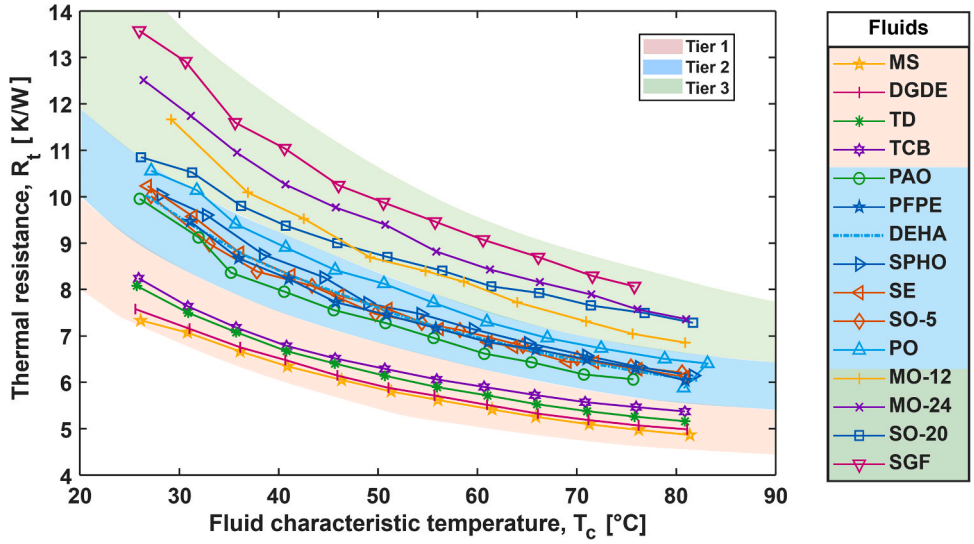


Fig. 9. Fluid characteristics of the tested dielectrics. Thermal resistance (R_t, Eq. 15) as a function of cooling liquid characteristic temperature. Uncertainty in the measured temperature difference and input power are smaller than the symbol sizes and are not shown for clarity. Lines connecting the data points are guiding lines only, and do not represent any statistical fit. See Table 1 for fluid symbol definition.

temperature difference range from 20℃ to 120℃. The detailed simulation setup, mesh independence, and validation are provided in Appendix A.

Fig. 10 shows the variation of the heat transfer coefficient on the copper drain tab with temperature difference for all the tested fluids. The heat transfer coefficient increases consistently with increasing temperature, primarily because reduced viscosity near the heated device surface promotes stronger buoyancy-driven natural convection flows. Since the bulk fluid is maintained nearly around 21°C by the external chiller, this natural convection loop is much stronger at higher junction temperatures since the induced convection circulation draws colder fluids from the bulk tank back to the device effectively increasing overall convective heat transfer. Tier 1 candidate fluids show the highest heat transfer coefficient approximately 15–20% improvement over Tier 2 and 40–50% higher performance relative to Tier 3. Within commercial fluids, Tier 2 outperform tier 3 by 20–30% corresponding to an overall lower thermal resistance range. For reference, the theoretical water natural convection heat transfer coefficient over a vertical plate calculated with the Churchill and Chu [72] correlation is roughly three to five times higher than the best dielectrics fluids tested, highlighting the superior thermal transport capability of water. However, water's electrical conductivity and risk of corrosion make it unsuitable for direct immersion cooling applications. While conformal insulation coating on electronic devices allows direct water-based cooling, such coatings introduce additional thermal resistance due to the lower thermal conductivity of the coating and affect the potential heat transfer benefits.

Fig. 11(a) shows the relationship between the theoretical figure of merit, FOM_t, with the inverse of the measured thermal resistance, $1/R_t$, across 9 of the selected fluids. The chosen fluids are the ones with known temperature-dependent properties. This relationship is linear and indicates that FOM_t can be correlated to the experimental measurements through a simple linear function, enabling the estimation of an experimental figure of merit, FOM_{exp}, from $1/R_t$. Each dataset begins at a surface temperature of approximately 30 °C (T_c = 25°C) and extends to

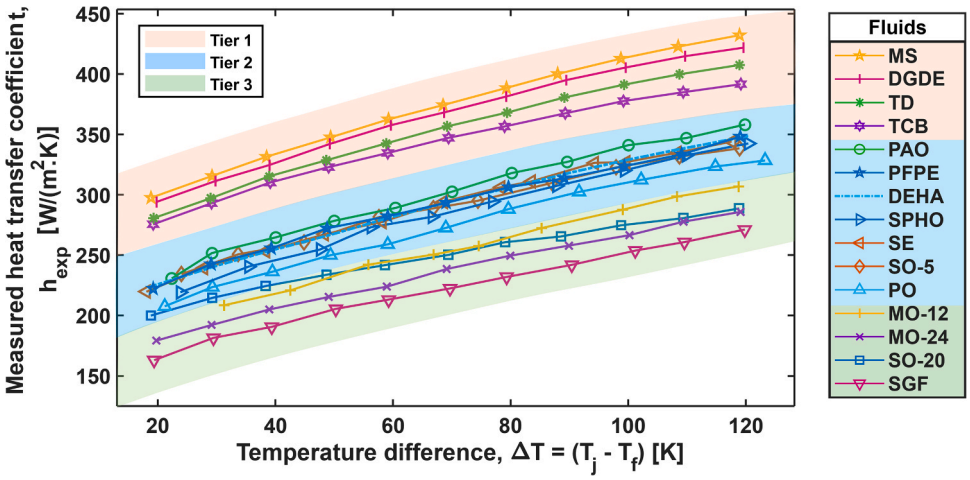


Fig. 10. Estimated heat transfer coefficient on the copper drain tab as a function of junction-to-fluid temperature difference or all 15 dielectric fluids. Lines connecting the data points are guiding lines only, and do not represent any statistical fit. See Table 1 for fluid symbol definition.

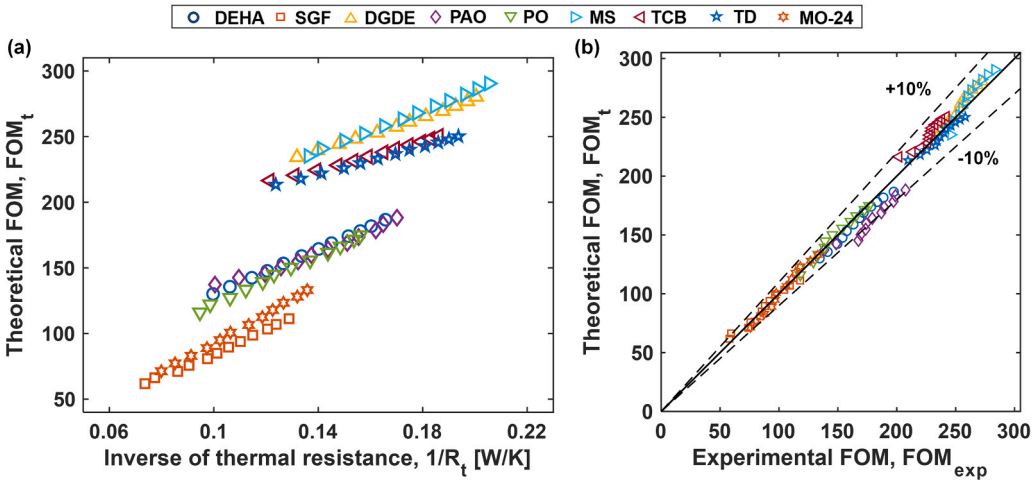


Fig. 11. Figure of merit comparison of the results: (a) Theoretical FOM derived from Eq. (5) vs the inverse of thermal resistance data for selective fluids, (b) Theoretical FOM derived from Eq. (5) vs the derived experimental FOM of corresponding fluids. See Table 1 for fluid symbol definition.

about 140°C (T_c = 80°C), showing that the slope varies for different fluids due to differences in temperature-dependent thermophysical properties. Meanwhile, the distinct FOM_t ranges among the fluids correspond to their performance tiers, where MS, DGDE, TCB, and TD are in the top tier, PAO, PO, and DEHA are in the mid-tier, and MO−24, and SGF at the lower end. These are all consistent with the trends observed previously in Fig. 9. Based on the relationship shown in Fig. 11 (a), an empirical correlation between the theoretical and experimental data is derived as

$$FOM_{exp} \approx a\left(\frac{1}{R_t}\right) + b, \tag{24}$$

$$a = 0.2178T_c^2 - 38.669T_c + 3865.4, \tag{25}$$

$$b = 0.003T_c^2 - 0.2666T_c - 158.66. \tag{26}$$

Fig. 11(b) compares the resulting FOM_{exp} with FOM_t, showing strong agreement within ±10% across all 9 fluids. This confirms the validity of using experimentally measured R_t to estimate FOM_t without requiring full property data with the change of temperature. Such a correlation is particularly valuable because obtaining complete temperature-dependent property data for commercial dielectric fluids and mixtures remains costly and time-consuming. The ability to directly infer FOM_{exp} from thermal resistance measurements allows rapid and consistent benchmarking of SPIC fluids. Moreover, while theoretical FOMs are intuitive and property-based, the experimental framework captures practical effects such as structural materials and heat-spreading characteristics of real electronic assemblies. Therefore, this correlation provides a robust link between experimental testing and theoretical evaluation offering a convenient pathway to assess, compare, and select dielectric fluids even when detailed material data are unavailable. In addition, the present framework can be extended to pumped SPIC configurations by incorporating controlled flow rates and pressure drop measurements.

Fig. 12 records the transient leakage current response when a voltage bias is first applied to the immersed, off-state Infineon device in SPHO. Three applied voltages of 100, 300, and 550 V were recorded, along with one where no bias was applied. For the non-zero biases, I_l shows a rapid initial decay over the first 10–30 s and approaches a quasi-steady plateau. The plateau level increases with applied voltage for about 1.2 nA at 100 V, 2 nA at 300 V, and 5 nA at 550 V. Even at 550 V, the currents remain in the single digit nA range, highlighting the high resistivity of SPHO liquid. The 0 V trace oscillates around zero and represents the measurement noise floor of the current leakage setup (instrumentation and cabling), setting the resolution of current leakage to 50 pA stated in Table 3. The average of the current leakage at each bias voltage was reported in Fig. 13 for every tested fluid.

Fig. 13 plots the closed switch leakage current for each fluid at

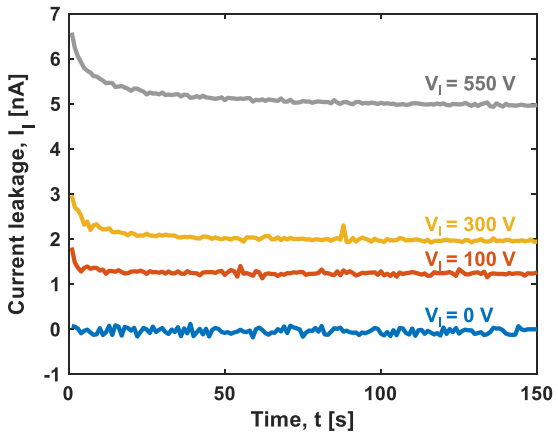


Fig. 12. Transient current leakage data for the SPHO liquid.

100 V, 300 V, and 550 V on a logarithmic scale. For most of the commercial candidates like silicon oils, SPHO, PAO, PO, MO−12, MO−24, SE, SGF, and TD, the bars lie below 10 nA at all different voltages applied. This consistent level of low current response is attributed to the intrinsic high resistivity of pure base oils (silicon, PFPE, white mineral oil) and the stabilizing effect of additive compounds (oxidation inhibitors or metal deactivators) in the formulated fluids. Collectively, these properties ensure robust dielectric behavior and minimal leakage even at the highest bias. In contrast, two fluids display markedly higher conduction. MS has the highest leakage at approximately 0.04 mA when 550 V is applied. The second one, TCB, exhibited approximately 0.1694 μA at 550 V. Overall, most fluids maintain tight leakage control across the operating range, whereas the polar or halogenated liquids (MS, DEHA, TCB) exhibit a steeper voltage sensitivity that could require additional insulation strategies in high voltage applications.

Table 4 summarizes the twin figures of merit for thermal and electrical performance, R_t at $\Delta T \approx 120$°C and I_l at 550 V, respectively. Amongst the tested fluids, the thermal resistance value ranges from 4.9 K/W for MS to 7.8 K/W for SGF, which indicates a large variation in heat dissipation capability for SPIC natural convection cooling while maintaining the same fluid bulk liquid temperature. While multiple fluids exhibit leakage current < 5 nA, thermally better performing organic fluids such as MS and TCB show significantly higher leakage current, which suggests limitations with dielectric insulation properties. Amongst other pure fluids, DEHA and DGDE exhibit relatively low

Table 4
Performance summary of tested dielectric fluids. Fluids are ordered in order of most to least promising candidates.

Dielectric Fluids	R_t [K/W] (T_c = 80°C)	Measured Heat transfer coefficient, h [W/(m²·K)] (T_c = 80°C)	I_l [nA] (V_l = 550 V)	Estimated Volume Resistivity, ρ [Ω·m] (V_{DS} = 550 V)
TD	5.2	407.08	4.5	5.6×10^{13}
PAO	5.9	355.82	5	1.0×10^{14}
PFPE	6.0	343.10	4.4	6.0×10^{13}
SPHO	6.1	339.47	4.8	3.4×10^{13}
SE	6.1	344.17	7.4	1.2×10^{13}
SO-5	6.2	338.50	3.7	1.0×10^{15}
PO	6.4	325.54	4.1	3.9×10^{13}
MO-12	6.9	306.87	3.9	2.2×10^{14}
MO-24	7.0	284.32	4.6	4.9×10^{13}
SO-20	7.2	286.89	3.8	3.0×10^{14}
SGF	7.8	267.96	12.2	5.2×10^{12}
DEHA	6.0	346.66	22.6	2.4×10^{12}
DGDE	5.0	421.28	34	1.5×10^{12}
TCB	5.4	390.752	169.4	2.7×10^{11}
MS	4.9	431.56	40,065.3	1.1×10^{9}

thermal resistance with lower leakage current values. TD offers the most favorable combination of low thermal resistance (5.2 K/W) and low leakage current (4.5 nA), making it a well-balanced performer amongst the pure fluids in both the thermal and electrical aspects involved in SPIC.

Furthermore, the volume resistivity of each fluid can be estimated from the measured leakage current values, providing a quantitative metric for comparing dielectric strength across candidates. The detailed methodology and corresponding resistivity calculations are provided in the Appendix B. Notably, according to the Open Compute Project (OCP) base specification for immersion fluids [86], a minimum volume resistivity of 10^9 Ω·m is recommended for dielectric fluids intended for data center immersion applications.

6. Conclusions

A systematic comparative analysis of 15 dielectric liquids for single-phase immersion cooling (SPIC) was conducted through combined thermal and electrical performance testing. The property sensitivity and weight-factor framework established here confirmed that maximizing liquid thermal conductivity and liquid density while minimizing liquid

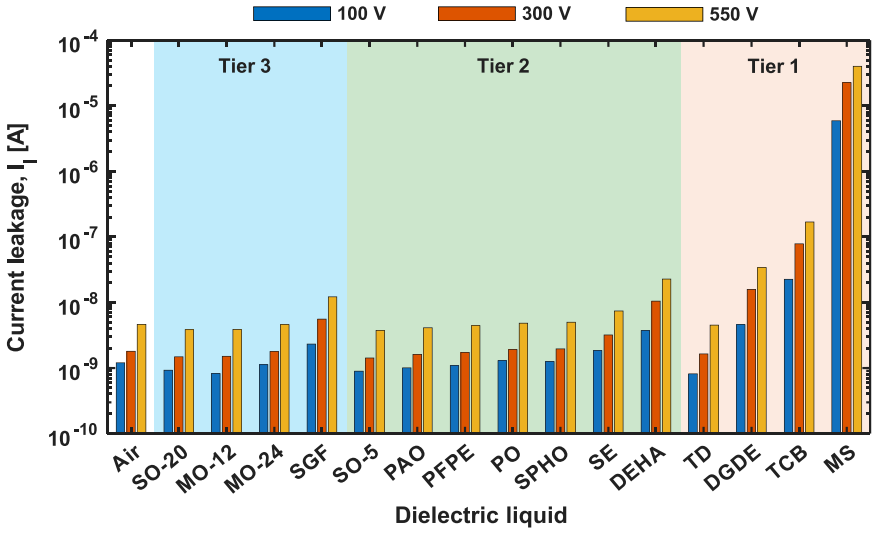


Fig. 13. Current leakage level comparison between dielectric fluids. See Table 1 for full details of the dielectric fluid properties. Uncertainty in the current leakage measurement was ± 0.05 nA, and is not plotted for clarity.

viscosity is critical to enhancing natural convection performance in SPIC systems. Experimental results demonstrated that liquids with inherently low dynamic viscosity and moderate to high thermal conductivity, such as methyl salicylate, tetradecane, and diethylene glycol dibutyl ether, achieved superior thermal resistance values under steady state conditions. Tier 1 candidate liquids showed characteristic thermal resistances of 4.9 - 5.4 K/W (2.32 – 2.56 (cm^2·K)/W), compared with 5.9 - 6.4 K/W (2.82 – 3.08 (cm^2·K)/W) for the best commercial tier 2 liquids (15–20% lower), and 7.0 - 7.8 K/W (3.27 – 3.75 (cm^2·K)/W) for tier 3 commercial options (30–36% lower). Electrical insulation measurements showed that the majority of commercial liquids maintained leakage currents of 3.7 −5 nA at 550 V, while certain polar or halogenated compositions exhibited higher electrical conduction. For example, 1,2,4-trichlorobenzene exhibited 169.4 nA of current leakage, and methyl salicylate was at 40,065.3 nA, which were 34-, and 8000-times higher relative to the 5 nA commercial liquid baseline, respectively, which highlights application dependent trade-offs in dielectric selection. Overall, the results emphasize that liquid choice has a significant impact on SPIC system performance and reliability, and the methodology presented here offers a robust pathway for evaluating and optimizing dielectric liquids for advanced electronics cooling applications.

CRediT authorship contribution statement

Shayan Aflatounian (equal): Writing – review & editing, Writing – original draft, Visualization, Validation, Software, Project administration, Methodology, Investigation, Formal analysis, Data curation, Conceptualization. **Sarath Subramaniyan (equal):** Writing – review & editing, Writing – original draft, Visualization, Validation, Software, Project administration, Methodology, Investigation, Formal analysis, Data curation, Conceptualization. **Kai Luo:** Writing – review & editing, Software, Project administration, Validation, Supervision, Investigation, Formal analysis, Data curation, Conceptualization. **Sujan Dewanjee:** Software, Methodology, Investigation, Data curation. **Vishwanath Ganesan:** Methodology, Investigation, Data curation, Formal analysis, Conceptualization, Visualization, Validation. **Oliver R. Gittus:** Investigation, Validation. **Erich A. Müller:** Supervision, Resources. **Giles Prentice:** Supervision, Resources. **Marc J Payne:** Supervision, Resources. **Andrew Stillwell:** Investigation, Resources, Supervision. **Paul V. Braun:** Investigation, Resources, Supervision. **Nenad Miljkovic:** Writing – review & editing, Validation, Supervision, Resources, Investigation, Formal analysis, Conceptualization.

Conflict of interest

The authors have no conflicts to disclose.

Declaration of Competing Interest

Given their role as Associate Editor, Nenad Miljkovic had no involvement in the peer-review of this article and has no access to information regarding its peer-review. Full responsibility for the editorial process for this article was delegated to another journal editor. If there are other authors, they declare that they have no known competing financial interests or personal relationships that could have appeared to influence the work reported in this paper.

Acknowledgements

This work was supported by Castrol and BP plc through the International Centre for Advanced Materials (ICAM). N.M. gratefully acknowledges funding support from the Air Conditioning and Refrigeration Center (ACRC), an NSF founded I/UCRC at UIUC and the International Institute for Carbon Neutral Energy Research (WPI-I2CNER), sponsored by the Japanese Ministry of Education, Culture, Sports, Science, and Technology.

Appendix A. Estimation of heat transfer coefficient

The vertical drain tab surface (12mm × 10.3mm) was selected as the reference area to estimate the heat transfer coefficient of the dielectric fluids. The coefficient was calculated using

$$h = \frac{Q_{Cu}}{A_{tab}(T_j - T_f)}, \tag{A.1}$$

where Q_{Cu} is the net heat dissipated through the drain tab and A_{tab} is the copper tab surface area. However, since there are other exposed surfaces of the device such as epoxy, and copper lead plate, in the total heat dissipation (Q) term, Q_{Cu} represents only a fraction of this total power dissipation.

To quantify this fraction, 3D steady state CFD simulations were conducted in ANSYS Fluent. Detailed structural and geometry information, including drain tab, epoxy package, solder, die, and PCB laminate based on manufacturer datasheet were incorporated to simulate a well-defined domain. The internal structure of the Infineon PG-HDSOP package used in this study is illustrated in Figure A1(a). The device consists of silicon die (5 mm × 8 mm × 0.08 mm), where volumetric heat generation is applied. The die is metallized with a top-side copper layer and mounted onto a copper lead frame (drain tab) both of which serve as the primary heat- spreading path. The assembly is encapsulated in an epoxy molding compound. The drain tab and source pins are soldered directly onto the PCB copper pads using standard reflow soldering. No additional thermal interface material was used between the device and PCB. Most of the heat transfer from the device is through top side copper, drain tab, epoxy, and copper solder. Two fluids, MS and DEHA with quite different thermal properties were chosen for this simulation. The dielectric fluid properties- density, viscosity, specific heat capacity, and thermal conductivity were defined as temperature dependent functions using the user defined.scm file to accurately capture property variation with temperature in the domain during simulation. The fluid-contacting walls were assigned a constant temperature boundary condition of 294.15 K to represent the externally chilled bulk fluid in the experiment. The die was defined as a volumetric heat source, with heat generation calculated from the electrical power input and die dimensions of 8mm × 5mm × 0.08mm. **Table A1** shows the summary of the simulation model.

The boundary conditions used in the natural convection thermal simulation as shown in **Table A1** include the initial ambient/ bulk temperature set to 294.15 K (21°C). External exposed surfaces were subjected to a convective heat transfer with uniform heat transfer coefficient of h = 10 W/(m^2·K). The bottom tank wall was modelled as an adiabatic wall. A constant temperature boundary condition of 294.14 K (21°C) was imposed on the interior walls of the tank to represent the ideal thermal sink condition maintained by the stainless-steel coiled heat exchanger surrounding the PCB in the experimental system. Volumetric heat generation as expressed by eq. (A.2), was applied with the silicon die (Vol = 5 mm ×8 mm ×0.08 mm).

$$q''' = \frac{Q}{Vol} \tag{A.2}$$

Table A1
Summary of the simulation parameters used in the ANSYS Fluent model.

Model setting	Description	Notes
Mesh	3427,365 poly- polyhedral elements, refined near the solid-fluid interface.	Validated by mesh independence.
Heat source	Volumetric heat source from the die inside the device.	Die size of 8 mm× 5 mm× 0.08 mm, given by the product info
Boundary conditions	1. Operating pressure of 1 atm 2. Constant fluid-contacting walls 3. Temperature boundary condition of 294.15 K *4.* $h = 10$ W/(m^2·K) for top and PCB outer walls 5. Adiabatic bottom wall	The constant temperature wall boundary approximates well-regulated thermal reservoir

Figure A1(a) shows the 3-D computational domain that consists of the Infineon power device with detailed internal layers including copper drain tab, solder, die, epoxy package frame, and PCB laminate immersed in the dielectric test fluid. **Figure A1**(b) shows the mesh and mesh refinement near the copper tab of interest. A polyhedral mesh was selected for this slightly complicated geometry to reduce solving time and improve accuracy. Local mesh sizing was applied individually to critical components of the package and the surrounding fluid domain, ensuring targeted refinement in regions where large gradients in temperature and velocity are possible. The simulations were conducted using a steady state, pressure-based solver in ANSYS Fluent under laminar flow conditions considering fluid as Newtonian and incompressible. Gravity was included to model buoyancy driven natural convection with thermophysical properties defined as fully temperature dependent functions to accurately capture temperature gradient effects in the system domain. The coupled pressure-velocity scheme was used with PRESTO! discretization for pressure and second order upwind schemes for momentum and energy equations. Convergence was verified through residual reduction below 10^{-3} and stabilization of maximum temperature of the silicon die and heat flux values.

The simulations were performed by solving the steady-state three-dimensional conservation equations for mass, momentum, and energy. The governing equations are solved in the domain are stated, along with the assumptions of steady-state, laminar, incompressible flow with temperature dependent thermophysical properties. Buoyancy effects were modeled by including gravity and fully temperature dependent density. These clarify mathematical framework of the methods used for modelling.

The temperature-dependent property correlations for density, thermal conductivity, specific heat capacity, viscosity, and thermal expansion coefficient are summarized in **Table A2**, **Table A3**, **Table A4**, **Table A5**, and **Table A6** respectively. These properties were used for the predictive analysis of the Churchill and Chu [72] shown in **Figure A4**. Only nine out of the 15 fluids experimentally evaluated fluids were chosen since complete temperature-dependent property correlations over the entire operating temperature range were available only for these fluids. This ensures a consistent and physically meaningful comparison between the model predictions and experimental data, particularly since these properties vary significantly with temperature, especially viscosity which strongly influences natural convection behavior.

Table A2
Density, ρ [kg/m^3] as a function of temperature, T [K].

Fluid Symbol	Density, ρ [$\mathbf{kg/m^3}$] as a function of temperature, T [**K**]	Reference
PAO	$-0.5547*T + 930.55$	[87]
PO	$-0.6691*T + 990.3$	
MO−24	$-0.6424*T + 1066.9$	[88]
SGF	$-0.2823*T + 1008.1$	[89]
TD	$\left(\frac{0.27248}{0.24007^{1+\left(1-\frac{T}{693}\right)^{0.28571}}}\right) * 198.388$	[90]
DEHA	$\left(\frac{0.1723}{0.24046^{\left(1+\left(1-\frac{T}{783.2}\right)^{0.28571}\right)}}\right) * 370.566$	
DGDE	$\left(\frac{0.3113}{0.24994^{1+\left(1-\frac{T}{680}\right)^{0.28571}}}\right) * 218.333$	

(*continued on next page*)

Table A2 (*continued*)

Fluid Symbol	Density, ρ [$\mathbf{kg/m^3}$] as a function of temperature, T [**K**]	Reference
TCB	$\left(\frac{0.61713}{\left(0.2524^{\left(1+\left(1-\frac{T}{725}\right)^{0.2857}\right)}\right)}\right) * 181.447$	
MS	$\left(\frac{0.64048}{\left(0.26242^{\left(1+\left(1-\frac{T}{709}\right)^{0.27235}\right)}\right)}\right) * 152.147$	

Table A3
Thermal conductivity, k [$W/(m{\cdot}K)$] as a function of temperature, T [K]

Fluid Symbol	Thermal conductivity, **k** [**W**/(**m**·**K**)] as a function of temperature, T [**K**]	Reference
PAO	$-0.0002{*}T + 0.1939$	[87]
PO	$-0.0002{*}T + 0.175$	
MO-24	$-8{*}10^{-5}{*}T + 0.1403$	[88]
SGF	$-1{*}10^{-4}{*}T + 0.2123$	[89]
TD	$0.0441122{*}\left(1 + 2.99248{*}\left(1-\frac{T}{693}\right)^{\frac{1}{3}} - 7.97743{*}\left(1-\frac{T}{693}\right)^{\frac{2}{3}} + 8.97743{*}\left(1-\frac{T}{693}\right)\right)$	[90]
DEHA	$0.048004{*}\left(1 + 2.2381{*}\left(1-\frac{T}{783.2}\right)^{\frac{1}{3}} - 5.7142{*}\left(1-\frac{T}{783.2}\right)^{\frac{2}{3}} + 6.7142{*}\left(1-\frac{T}{783.2}\right)\right)$	
DGDE	$0.19673 - 0.0001708{*}T$	
TCB	$0.1144981 - 0.00011083{*}T$	
MS	$0.20533 - 0.00020728{*}T$	

Table A4
Specific heat capacity, c_p [$J/(kg{\cdot}K)$] as a function of temperature, T [K]

Fluid Symbol	Specific heat capacity, $\mathbf{c_p}$ [**J**/(**kg**·**K**)] as a function of temperature, T [**K**]	Reference
PAO	$2.0566{*}T + 1411.9$	[87]
PO	$3.1533{*}T + 897.55$	
MO-24	$4.4813{*}T + 508.59$	[88]
SGF	$1.0393{*}T + 1653$	[89]
TD	$\frac{353140 + 29.13{*}T + 0.86116{*}T^2}{198.388}$	[90]
DEHA	$\frac{\left(985370 + \frac{14338}{1-\frac{T}{783.2}} + 466840{*}\left(1-\frac{T}{783.2}\right) - 2954500{*}\left(1-\frac{T}{783.2}\right)^2 + 2250600{*}\left(1-\frac{T}{783.2}\right)^3\right)}{370.566}$	
DGDE	$\frac{204000 + 759{*}T}{218.333}$	
TCB	$\frac{126810 + 220.94{*}T}{181.447}$	
MS	$\frac{41091 + 692.32{*}T}{152.147}$	

Table A5
Viscosity μ [$mPa{\cdot}s$] as a function of temperature, T [K].

Fluid Symbol	Viscosity, **μ** [**mPa·s**] as a function of temperature, T [**K**]	Reference
PAO	$1.049{*}10^{-6}{*}\exp\left(\frac{2582.32}{T}\right)$	[87]
PO	$1.01{*}10^{-6}{*}\exp\left(\frac{2486}{T}\right)$	
MO−24	$1.52{*}10^{-6}{*}\exp\left(\frac{2796}{T}\right)$	[88]
SGF	$2.83{*}10^{-6}{*}\exp\left(\frac{2987}{T}\right)$	[89]
TD	$\exp\left(-136.73+\frac{6421.3}{T}+19.493{*}\ln(T)-2.297{*}10^{-5}{*}T^2\right)$	[90]
DEHA	$\exp\left(17.748-\frac{761.484}{T}-3.8677{*}\ln(T)+1.87166{*}10^{10}{*}T^{-4}\right)$	
DGDE	$\exp(-3.0183+\frac{1198.4}{T}-1.2578{*}\ln(T))$	
TCB	$\exp\left(-243.59+\frac{9989.7}{T}+36.519{*}\ln(T)-4.7943{*}10^{-5}{*}T^2\right)$	
MS	$\exp\left(-27.698+\frac{2484.8}{T}+2.3513{*}\ln(T)\right)$	

Table A6
Thermal expansion coefficient, $\beta\,[1/K]$ as a function of temperature, T [K].

Fluid Symbol	Thermal expansion coefficient, **β** [**1/K**] as a function of temperature, T [**K**]	Reference
PAO	$5.7526340493{*}\,10^{-7}{*}T+\,7.0962547731{*}\,10^{-4}$	[87]
PO	$7.9610843386{*}\,10^{-7}{*}T+\,8.2468025281{*}\,10^{-4}$	
MO−24	$5.9019290275{*}\,10^{-7}{*}T+\,7.1813781079{*}\,10^{-4}$	[88]
SGF	$9.6899092846{*}\,10^{-8}{*}T+\,3.0305403070{*}\,10^{-4}$	[89]
TD	$2.1476869992\,{*}\,10^{-6}{*}T+\,8.1422317283\,{*}\,10^{-4}$	[90]
DEHA	$1.3669145149{*}\,10^{-6}{*}T+\,6.9220876464\,{*}\,10^{-4}$	
DGDE	$2.2491101367\,{*}\,10^{-6}{*}T+\,8.1130702198\,{*}\,10^{-4}$	
TCB	$1.7441467313\,{*}\,10^{-6}{*}T+\,7.4008372709\,{*}\,10^{-4}$	
MS	$1.8077246705\,{*}\,10^{-6}{*}T+\,7.1005418993\,{*}\,10^{-4}$	

The simulated results for DEHA at 18 W power input illustrate a clear buoyancy-driven convection pattern above the drain tab as shown in **Figure A1**(c) with which clearly illustrates the strong thermal gradients formed near the drain tab surface relative to the bulk fluid temperature based on input boundary conditions. Three vertical plumes forming from the device center and the solder patch on either side of the package. **Figure A1**(d) represents the velocity field in the direction perpendicular to the device-PCB assembly, which shows a defined upward jet along the front of the device. The rear side of the PCB has a slightly slower jet due to lower thermal conductivity of the PCB, which creates a temperature gradient from the device-mounted side to the rear surface.

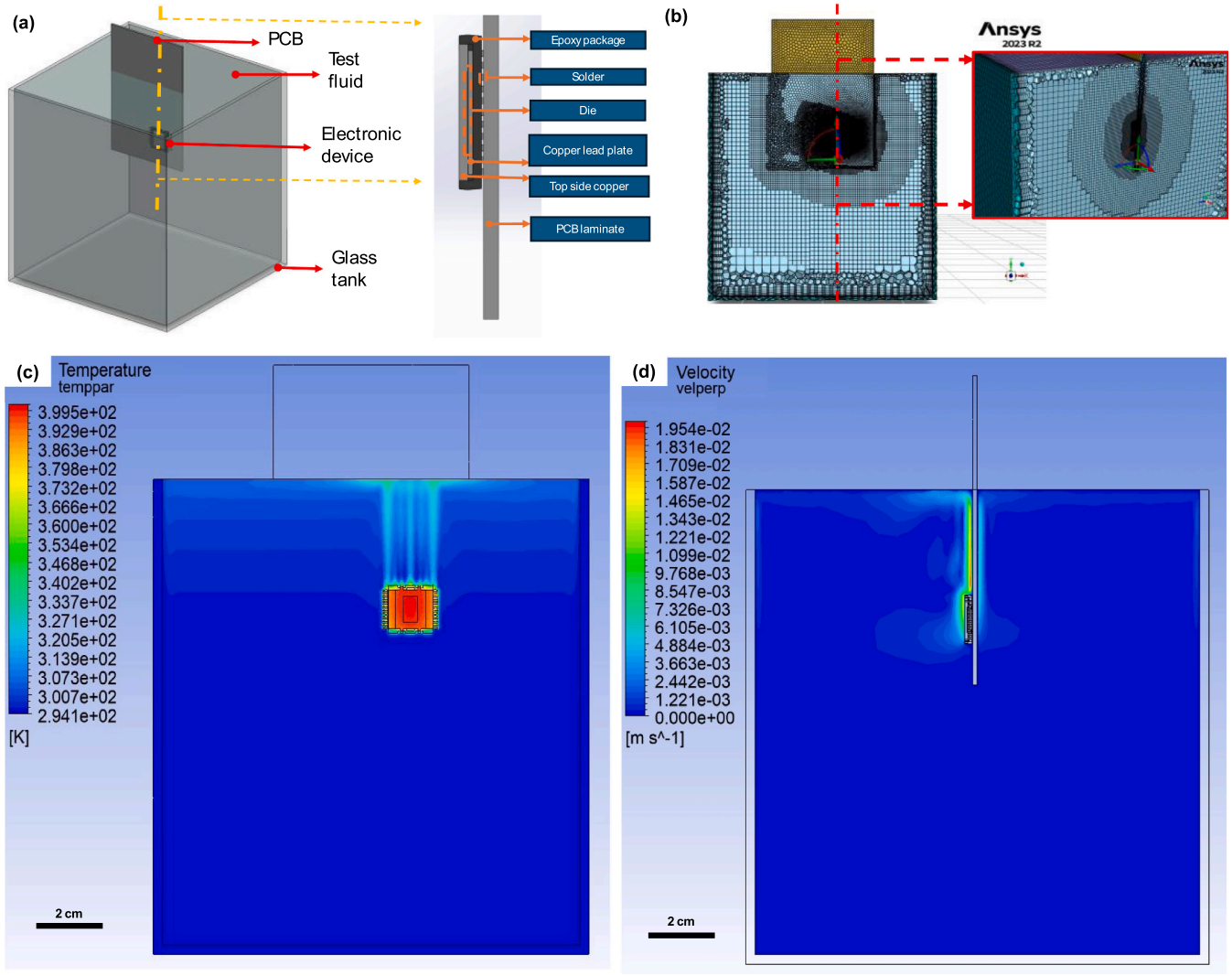


Fig. A1. (a) Three-dimensional simulation domain showing the immersed power device and surrounding fluid region with detailed cross-sectional view of the device stack, and (b) corresponding mesh with mesh refinement in the solid–fluid interface region. (c) Simulated steady-state temperature distribution across the device and surrounding fluid-DEHA at 18 W. (d) Corresponding velocity field showing natural convection around the heated device.'.

.

Figure A2 presents the mesh independence study for the fraction of total heat dissipated through the drain tab (Q_{Cu}/Q) as a function of the number of mesh elements. Q_{Cu} is obtained by calculating the total heat from the drain tab surface. This is computed by using the local heat flux value over the tab area estimated from the simulation. The solution converges beyond approximately 1.7 million elements with maximum variation in fraction less than 0.93% satisfying 1% mesh convergence criteria for the chosen mesh size of approximately 3.4 million elements as highlighted in **Figure A2** and detailed in **Table A1**.

Figure A3 shows the validation of the CFD model against experimental data for the two fluids DEHA and MS. The simulated junction-to-fluid temperature rise matches closely with experimental data, with an average deviation of less than 7% across the testes power range. The minor deviations between numerical and experimental results for DEHA may arise from experimental uncertainties, sensitivity of natural convection to temperature dependent properties such as viscosity, and the idealized boundary condition assumptions in the CFD model. Since DEHA exhibits stronger viscosity variation with temperature than MS, small property deviations can lead to amplified differences in predicted buoyancy driven heat transfer. This agreement confirms that the model effectively captures both the conduction through different layers of the electronic device package and natural convection driven by temperature-dependent fluid properties for the selected fluids.

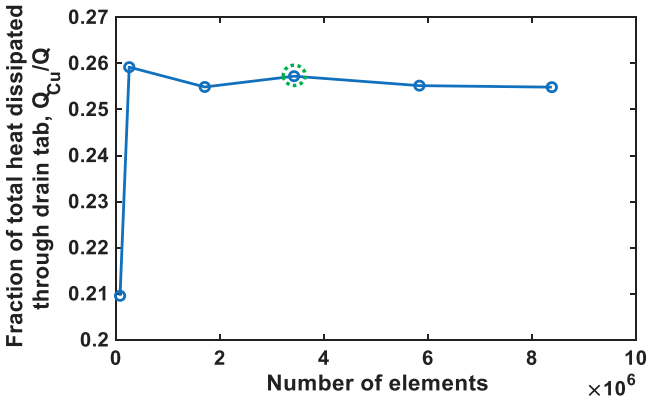


Fig. A2. Mesh independence study showing the fraction of total heat dissipated through the drain tab (Q_{Cu}/Q) as a function of the number of mesh elements. The dashed circle shows the mesh used for analysis.

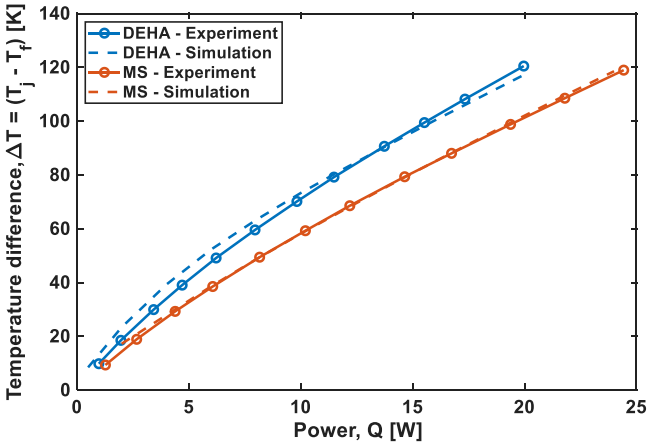


Fig. A3. Comparison between experimental and simulated junction to ambient temperature rise as a function of heating power for 2 dielectric fluids DEHA and MS.

.

Results from the fluids indicate that Q_{Cu} accounts for approximately 25–27% of the total power input, with minor variation at higher junction temperature. As seen in **Figure A4**, the simulated heat dissipation fraction nearly remains constant with increasing temperature difference, which confirms the relative contribution by the copper drain tab to heat removal is largely independent of the operating power. Accordingly, a general correlation for estimating the heat dissipation through the copper tab is given in eq. (A.4), with an accuracy of ± 3% for both MS and DEHA across the tested temperature range.

$$Q_{Cu} = 0.26Q \ . \tag{A.4}$$

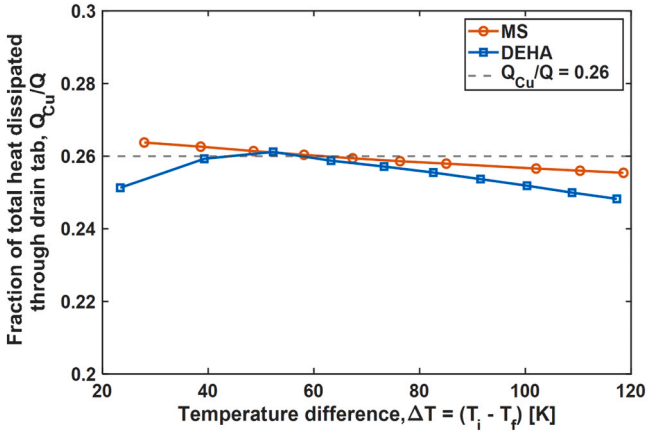


Fig. A4. Variation of simulated heat dissipation fraction through the copper drain tab, Q_{Cu}/Q, against junction to ambient temperature difference for DEHA and MS dielectric fluids. The dashed line a represents the $Q_{Cu}/Q = 0.26$ correlation chosen for the average heat fraction used for calculating the estimated heat transfer coefficient.

.

Based on this modification of the $Q_{Cu} = 0.26Q$, we validate this estimation method by comparing the experimental HTC ($h_{Exp.}$) with the predicted HTC ($h_{Pred.}$) from the Churchill and Chu [72] correlation for natural convection of vertical surfaces using Eq. (4) for a constant heat flux boundary condition. Evaluating the thermophysical properties of the dielectric liquids at liquid film temperature, the predictive capability of the Churchill and Chu [72] correlation is shown in **Figure A5** for nine liquids spanning all three tiers, viz., Tier 1 (TCB, MS, TD, and DGDE), Tier 2 (PO, PAO, and DEHA), and Tier 3 (SGF and MO−24). For this analysis, only the 9 fluids used in Fig. 11 with accurately known temperature-dependent thermophysical properties obtained from the manufacturer or literature sources were considered to ensure a reliable comparison. For the combined liquid dataset with 108 data points, with a mean absolute error (MAE) of 10.2%, this correlation captures 88% and 97% of the data within ±20% error and ±30% error, respectively.

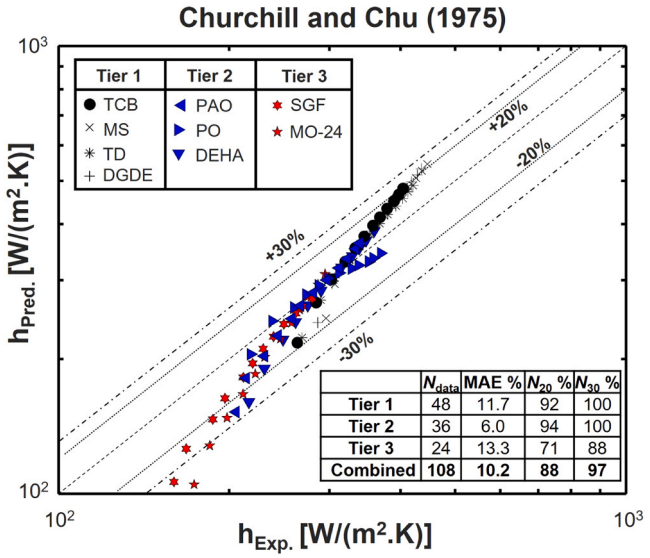


Fig. A5. Predictive capabilities of the Churchill and Chu [72] correlation in estimating the single-phase natural convection heat transfer coefficient on flat vertical heated surfaces immersed in Tier 1, 2, and 3 of the dielectric liquids.

.

Appendix B. . Estimation of fluid volume resistivity

In this study, there are two pathways in parallel for the current leakage, including the transistor and the fluid. **Figure B1** shows the schematic of the circuit for the current leakage test.

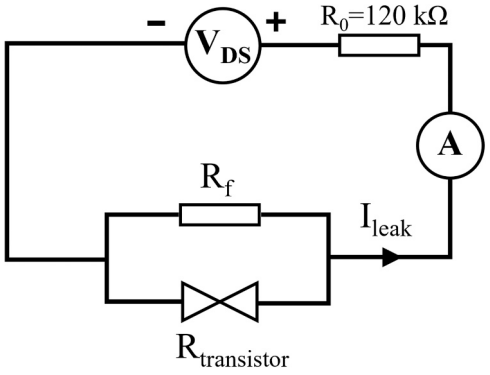


Fig. B1. Schematic of the circuit loop used for the current leakage test.

.

The measured current leakage I_{leak} can be expressed as

$$I_{leak} = \frac{V_{DS}}{\frac{1}{\left(\frac{1}{R_{transistor}}+\frac{1}{R_f}\right)} + R_0} \quad , \tag{B.1}$$

where V_{DS} is the applied voltage, R_0 is the protection resistance (120 kΩ) in the circuit, $R_{transistor}$ is the resistance of the transistor, and R_f is the resistance of the fluid. The volume resistivity (ρ_f) of the fluid can be expressed as

$$\rho_f = \frac{A}{l} R_f \ , \tag{B.2}$$

where A and l are the cross-sectional area and length of the current leakage path through the fluid, respectively.

Given the device geometries, it is difficult to determine the exact cross-sectional area and length of the current leakage path. Instead, an effective value of l/A is estimated by assuming:

1) The transistor resistance, $R_{transistor}$, is only dependent on the device characteristics and applied voltage and device and does not change when immersed in different fluids.
2) The effective current leakage pathway remains the same for different fluids.

If the volume resistivities of two fluids are known, the current leakages of the two fluids under the same drain-source voltage can be calculated as

$$I_{leak,1} = \frac{V_{DS}}{\frac{1}{\left(\frac{1}{R_{transistor}} + \frac{A}{l}\frac{1}{\rho_{f,1}}\right)} + R_0} \ , \tag{B.3}$$

$$I_{leak,2} = \frac{V_{DS}}{\frac{1}{\left(\frac{1}{R_{transistor}} + \frac{A}{l}\frac{1}{\rho_{f,2}}\right)} + R_0} \ , \tag{B.4}$$

where the subscripts 1 and 2 refer to two different fluids. Combining Eqs. B.3 and B.4, the effective value l/A can be expressed as

$$\left(\frac{l}{A}\right)_{eff} = \frac{\left(\frac{1}{\rho_{f,1}} - \frac{1}{\rho_{f,2}}\right)}{\frac{1}{\frac{V_{DS}}{I_{leak,1}} - R_0} - \frac{1}{\frac{V_{DS}}{I_{leak,2}} - R_0}} \ . \tag{B.5}$$

Among the fluids tested in this study, the volume resistivities of silicon oil (5 cSt) [91] and Perfluorinated polyether fluid [92] are given by the manufacturers as $\rho_{f,1} = 1 \times 10^{15}$ Ω·m and $\rho_{f,2} = 6 \times 10^{13}$ Ω·m, respectively. Based on the measured current and drain-source voltage, the effective value of l/A is estimated to be 0.0123 m^{-1}.

Finally, other volume resistivities of the tested fluid can be estimated as

$$\rho_{f,i} = \frac{1}{\left(\frac{l}{A}\right)_{eff}\left[\frac{1}{\frac{V_{DS}}{I_{leak,i}} - R_0} - \frac{1}{\frac{V_{DS}}{I_{leak,1}} - R_0}\right] + \frac{1}{\rho_{f,1}}} \ , \tag{B.6}$$

where the subscript i refers to the fluids with unknown volume resistivity.

Data Availability

Data will be made available on request.

References

[1] G.A. Brady, N. Kapur, J.L. Summers, and H.M. Thompson, A case study and critical assessment in calculating power usage effectiveness for a data centre", doi: 10.1016/j.enconman.2013.07.035.

[2] J. Tian, C. Lai, G. Feng, D. Banerjee, W. Li, N.C. Kar, Review of recent progresses on gallium nitride transistor in power conversion application, Int. J. Sustain. Energy 39 (1) (2020) 88–100, https://doi.org/10.1080/14786451.2019.1657866.

[3] K. Ebrahimi, G.F. Jones, A.S. Fleischer, A review of data center cooling technology, operating conditions and the corresponding low-grade waste heat recovery opportunities, Renew. Sustain. Energy Rev. 31 (2014) 622–638, https://doi.org/10.1016/J.RSER.2013.12.007.

[4] S.N. Joshi, et al., A review of select patented technologies for cooling of high heat flux power semiconductor devices, IEEE Trans. Power Electron 38 (6) (2023) 6790–6794, https://doi.org/10.1109/TPEL.2023.3243546.

[5] J. Zhang, L. Zhang, F. Sun, Z. Wang, An overview on thermal safety issues of lithium-ion batteries for electric vehicle application, IEEE Access 6 (2018) 23848–23863, https://doi.org/10.1109/ACCESS.2018.2824838.

[6] L. He, Z. Gu, Y. Zhang, H. Jing, P. Li, Review on thermal management of lithium-ion batteries for electric vehicles: advances, challenges, and outlook, Energy Fuels 37 (7) (2023) 4835–4857, https://doi.org/10.1021/acs.energyfuels.2c04243.

[7] H.M.R. Campelo, X.M. Lopez-Fernandez, P. Picher, and F. Torriano, Advanced Thermal Modelling Techniques in Power Transformers. Review and Case Studies.".

[8] M. Andresen, K. Ma, G. De Carne, G. Buticchi, F. Blaabjerg, M. Liserre, Thermal stress analysis of medium-voltage converters for smart transformers, IEEE Trans. Power Electron 32 (6) (2017) 4753–4765, https://doi.org/10.1109/TPEL.2016.2600270.

[9] E.M. Dede, et al., Techno-economic feasibility analysis of an extreme heat flux micro-cooler, iScience 26 (1) (2023) 105812, https://doi.org/10.1016/j.isci.2022.105812.

[10] Q. Zhang, et al., A survey on data center cooling systems: technology, power consumption modeling and control strategy optimization, J. Syst. Arch. 119 (2021) 1383–7621, https://doi.org/10.1016/j.sysarc.2021.102253.

[11] "Energy demand from AI – Energy and AI – Analysis, IEA. Accessed: Aug. 09, 2025. [Online]. Available: ⟨https://www.iea.org/reports/energy-and-ai/energy-demand-from-ai⟩.

[12] "El Capitan: NNSA's first exascale machine | Advanced Simulation and Computing." Accessed: Aug. 09, 2025. [Online]. Available: ⟨https://asc.llnl.gov/exascale/el-capitan⟩.

[13] "NREL Joins $40 Million Effort To Advance Data Center Cooling Efficiency | NREL." Accessed: Aug. 09, 2025. [Online]. Available: ⟨https://www.nrel.gov/news/detail/program/2023/nrel-joins-effort-to-advance-data-center-cooling-efficiency⟩.

[14] by S. S. ANANDAN and V. Ramalingam, THERMAL MANAGEMENT OF ELECTRONICS: A REVIEW OF LITERATURE, vol. 12, pp. 5–26, 2008, doi: 10.2298/TSCI0802005A.

[15] S.V. Garimella, L.-T. Yeh, T. Persoons, S.V. Garimella, L.-T. Yeh, and T. Persoons, Thermal Management Challenges in Telecommunication Systems and Data Centers, 2012, doi: 10.1109/TCPMT.2012.2185797.

[16] Z. Zhang, X. Wang, Y. Yan, A review of the state-of-the-art in electronic cooling, E-Prime - Adv. Electr. Eng. Electron. Energy 1 (2021) 100009, https://doi.org/10.1016/J.PRIME.2021.100009.

[17] A.L. Moore, L. Shi, Emerging challenges and materials for thermal management of electronics, Mater. Today 17 (4) (2014) 163–174, https://doi.org/10.1016/j.mattod.2014.04.003.

[18] A. Capozzoli and G. Primiceri, Cooling systems in data centers: state of art and emerging technologies, vol. 83, pp. 484–493, 2015, doi: 10.1016/j.egypro.2015.12.168.

[19] H.M. Daraghmeh and C.-C. Wang, A review of current status of free cooling in datacenters, 2016, doi: 10.1016/j.applthermaleng.2016.10.093.

[20] S.V. Patankar, Airflow and cooling in a data center, J. Heat. Transf. 132 (7) (Jul. 2010) 1–17, https://doi.org/10.1115/1.4000703/451420.

[21] J. Cho, S. Kim, Evaluation of air management system's thermal performance for superior cooling efficiency in high-density data centers, Energy Build. 43 (2011) 2145–2155, https://doi.org/10.1016/j.enbuild.2011.04.025.

[22] H. Zhang, S. Shao, H. Xu, H. Zou, and C. Tian, Free cooling of data centers: A review", doi: 10.1016/j.rser.2014.04.017.

[23] S. Xu, H. Zhang, Z. Wang, S. Xu, H. Zhang, Z. Wang, Thermal management and energy consumption in air, liquid, and free cooling systems for data centers: a review, *2023 Vol 16 Page 1279*, Energ 16 (3) (2023) 1279, https://doi.org/10.3390/EN16031279.

[24] A. Datta, D. Sanyal, A. Agrawal, A.K. Das, A review of liquid flow and heat transfer in microchannels with emphasis to electronic cooling, Sadhana - Acad. Proc. Eng. Sci. 44 (12) (2019) 1–32, https://doi.org/10.1007/S12046-019-1201-2/TABLES/7.

[25] W. Zhou, et al., Research progress of the liquid cold plate cooling technology for server electronic chips: A review, Int. J. Energy Res 46 (9) (2022) 11574–11595, https://doi.org/10.1002/ER.7979.

[26] G. Zhao, X. Wang, M. Negnevitsky, and C. Li, An up-to-date review on the design improvement and optimization of the liquid-cooling battery thermal management system for electric vehicles, 2022, doi: 10.1016/j.applthermaleng.2022.119626.

[27] S.G. Kandlikar, C.N. Hayner, Liquid cooled cold plates for industrial high-power electronic devices—thermal design and manufacturing considerations, Heat. Transf. Eng. 30 (12) (2009) 918–930, https://doi.org/10.1080/01457630902837343.

[28] J. Gullbrand, M.J. Luckeroth, M.E. Sprenger, C. Winkel, Liquid cooling of compute system, J. Electron. Packag. Trans. ASME 141 (1) (2019), https://doi.org/10.1115/1.4042802/367391.

[29] Y. Yu, M. Chen, S. Zaman, S. Xing, M. Wang, H. Wang, Thermal management system for liquid-cooling PEMFC stack: from primary configuration to system control strategy, eTransportation 12 (2022) 100165, https://doi.org/10.1016/J.ETRAN.2022.100165.

[30] M.H. Mousa, N. Miljkovic, K. Nawaz, Review of heat transfer enhancement techniques for single phase flows, Renew. Sustain. Energy Rev. 137 (2021) 110566, https://doi.org/10.1016/j.rser.2020.110566.

[31] M.H. Mousa, C.-M. Yang, K. Nawaz, N. Miljkovic, Review of heat transfer enhancement techniques in two-phase flows for highly efficient and sustainable cooling, Renew. Sustain. Energy Rev. 155 (2022) 111896, https://doi.org/10.1016/j.rser.2021.111896.

[32] H. Qiu, et al., Scalably etched large footprint copper cold plates for high-power dissipation in data centers using R1233zd(E), Int. J. Heat. Mass Transf. 256 (2026) 127938, https://doi.org/10.1016/j.ijheatmasstransfer.2025.127938.

[33] I. Pinkus, et al., Ultra-low thermal resistance and pressure drop copper and copper-tungsten diamond-shaped pin fin cold plates for liquid cooling of electronics, Int. J. Heat. Mass Transf. 256 (2026) 128080, https://doi.org/10.1016/j.ijheatmasstransfer.2025.128080.

[34] O.M. Zaki, W.Y. Park, I. Pinkus, W.P. King, N. Miljkovic, Metal additively manufactured wavy fin cold-plate architecture for improved thermal-hydraulic performance, Int. J. Heat. Mass Transf. 256 (2026) 128138, https://doi.org/10.1016/j.ijheatmasstransfer.2025.128138.

[35] E. OrÓ, R. Allepuz, I. Martorell, and J. Salom, Design and economic analysis of liquid cooled data centres for waste heat recovery: A case study for an indoor swimming pool, 2017, doi: 10.1016/j.scs.2017.10.012.

[36] K. Haghshenas, B. Setz, Y. Blosch, M. Aiello, Enough hot air: the role of immersion cooling, Energy Inf. 6 (1) (2023) 1–18, https://doi.org/10.1186/S42162-023-00269-0/TABLES/3.

[37] A.E. Bergles, A. Bar-Cohen, Immersion Cooling of Digital Computers, Cool. Electron. Syst. (1994) 539–621, https://doi.org/10.1007/978-94-011-1090-7_23.

[38] P.E. Tuma, The merits of open bath immersion cooling of datacom equipment, Annu. IEEE Semicond. Therm. Meas. Manag. Symp. (2010) 123–131, https://doi.org/10.1109/STHERM.2010.5444305.

[39] C. Zhang, H. Wang, Y. Huang, L. Zhang, Y. Chen, Immersion liquid cooling for electronics: Materials, systems, applications and prospects, Renew. Sustain. Energy Rev. 208 (2025) 114989, https://doi.org/10.1016/j.rser.2024.114989.

[40] P. Birbarah *et al.*, Water immersion cooling of high power density electronics, 2019, doi: 10.1016/j.ijheatmasstransfer.2019.118918.

[41] Z. Liu, et al., Machine learning enhanced control co-design optimization of an immersion cooled battery thermal management system, J. Appl. Phys. 136 (2) (2024) 025001, https://doi.org/10.1063/5.0201438.

[42] S. Zheng, et al., A comprehensive review of single-phase immersion cooling in data centres, Appl. Therm. Eng. 272 (2025) 126385, https://doi.org/10.1016/j.applthermaleng.2025.126385.

[43] T. Gebrael, et al., High-efficiency cooling via the monolithic integration of copper on electronic devices, Nat. Electron 5 (6) (2022) 394–402, https://doi.org/10.1038/s41928-022-00748-4.

[44] H. Qiu *et al.*, Single-Phase and Two-Phase Liquid Immersion Cooling of Data Center Power Supply Units for Heat Capture, in 2024 23rd IEEE Intersociety Conference on Thermal and Thermomechanical Phenomena in Electronic Systems (ITherm), May 2024, pp. 1–8. doi: 10.1109/ITherm55375.2024.10709424.

[45] C.H. Hoang, et al., A review of recent developments in pumped two-phase cooling technologies for electronic devices, IEEE Trans. Compon. Packag. Manuf. Technol. 11 (10) (2021) 1565–1582, https://doi.org/10.1109/TCPMT.2021.3117572.

[46] I.W. Kuncoro, N.A. Pambudi, M.K. Biddinika, I. Widiastuti, M. Hijriawan, K. M. Wibowo, Immersion cooling as the next technology for data center cooling: a review, J. Phys. Conf. Ser. 1402 (4) (2019) 044057, https://doi.org/10.1088/1742-6596/1402/4/044057.

[47] M.S. Patil, J.H. Seo, M.Y. Lee, A novel dielectric fluid immersion cooling technology for Li-ion battery thermal management, Energy Convers. Manag 229 (2021) 113715, https://doi.org/10.1016/J.ENCONMAN.2020.113715.

[48] Y. Huang, J. Ge, Y. Chen, C. Zhang, Natural and forced convection heat transfer characteristics of single-phase immersion cooling systems for data centers, Int. J. Heat. Mass Transf. 207 (2023) 124023, https://doi.org/10.1016/J.IJHEATMASSTRANSFER.2023.124023.

[49] J.R. Saylor, T.Y. Lee, T.W. Simon, W. Tong, P.S. Wu, A. Bar-Cohen, Fluid selection and property effects in single-and two-phase immersion cooling, IEEE Trans. Compon. Hybrids Manuf. Technol. 11 (4) (1988) 557–565, https://doi.org/10.1109/33.16697.

[50] S. Shao, T. Gao, H. Yang, J. Zhao, J. Zhang, Numerical analysis of oil immersion cooling of a server using mineral oil and Al2O3 nanofluid, ASME 2020 Int. Tech. Conf. Exhib. Packag. Integr. Electron. Photon. Microsyst. Inter. 2020 (2020), https://doi.org/10.1115/IPACK2020-2662.

[51] H. Shrigondekar, Y.C. Lin, C.C. Wang, Investigations on performance of single-phase immersion cooling system, Int. J. Heat. Mass Transf. 206 (2023) 123961, https://doi.org/10.1016/J.IJHEATMASSTRANSFER.2023.123961.

[52] X. Kang, Y. Wang, Q. Huang, Y. Cui, X. Shi, Y. Sun, Study on direct-contact phase-change liquid immersion cooling dense-array solar cells under high concentration ratios, Energy Convers. Manag 128 (2016) 95–103, https://doi.org/10.1016/J.ENCONMAN.2016.09.073.

[53] N.A. Pambudi, A.M. Yusuf, A. Sarifudin, The use of single-phase immersion cooling by using two types of dielectric fluid for data center energy savings, Energy Eng. 119 (1) (2021) 275–286, https://doi.org/10.32604/EE.2022.017356.

[54] M.R.H. Roni, et al., Enhanced surfaces manufactured using pulsed laser texturing for highly efficient two-phase cooling, Appl. Therm. Eng. 288 (2026) 129497, https://doi.org/10.1016/j.applthermaleng.2025.129497.

[55] Y. Wang, C. Wen, Q. Huang, X. Kang, M. Chen, H. Wang, Performance comparison between ethanol phase-change immersion and active water cooling for solar cells in high concentrating photovoltaic system, Energy Convers. Manag 149 (2017) 505–513, https://doi.org/10.1016/J.ENCONMAN.2017.07.054.

[56] A. Ristic-Smith, D.J. Rogers, Compact two-phase immersion cooling with dielectric fluid for PCB-based power electronics, IEEE Open J. Power Electron 5 (2024) 1107–1118, https://doi.org/10.1109/OJPEL.2024.3432989.

[57] J. Yao, Z. Hu, C.-H. Yen, C. Duan, A. Sachdev, M. Liu, Two-phase immersion cooling system with integrated condenser for power module cooling in EV applications, Appl. Therm. Eng. 278 (2025) 127226, https://doi.org/10.1016/j.applthermaleng.2025.127226.

[58] S. Dash, L. Rapoport, K.K. Varanasi, Crystallization-induced fouling during boiling: formation mechanisms to mitigation approaches, Langmuir 34 (3) (2018) 782–788, https://doi.org/10.1021/acs.langmuir.7b02936.

[59] D. Kang, J. Lee, A. Chakraborty, S.-E. Lee, G. Kim, C. Yu, Recent advances in two-phase immersion cooling with surface modifications for thermal management, Energies 15 (3) (Jan. 2022) 1214, https://doi.org/10.3390/en15031214.

[60] F. Spyrakis, T.A. Dragani, The EU's Per- and Polyfluoroalkyl Substances (PFAS) ban: a case of policy over Science, Toxics 11 (9) (2023) 721, https://doi.org/10.3390/toxics11090721.

[61] I.W. Kuncoro, N.A. Pambudi, M.K. Biddinika, I. Widiastuti, M. Hijriawan, K. M. Wibowo, Immersion cooling as the next technology for data center cooling: a review, J. Phys. Conf. Ser. 1402 (4) (2019) 044057, https://doi.org/10.1088/1742-6596/1402/4/044057.

[62] Y. Chen, et al., Experimental studies of saturated pool boiling heat transfer and critical heat flux on scalable etched copper surfaces for R-134a and low-GWP refrigerants R-1336mzz(E) and R-1336mzz(Z, Int. J. Heat. Mass Transf. 246 (Aug. 2025) 126958, https://doi.org/10.1016/j.ijheatmasstransfer.2025.126958.

[63] P. Warrier, A. Sathyanarayana, D.V. Patil, S. France, Y. Joshi, and A.S. Teja, Novel heat transfer fluids for direct immersion phase change cooling of electronic systems," 2012, doi: 10.1016/j.ijheatmasstransfer.2012.02.063.

[64] P.K.W. Harikumar Warrier, Design and evaluation of heat transfer fluids for direct immersion cooling of electronic systems (Ph.D.), Georgia Institute of Technology,, United States – Georgia, 2012, ⟨https://www.proquest.com/docview/1151124873/abstract/1A4CB77EBE254B82PQ/1⟩.

[65] A.J. Robinson, Status of Liquid Cooling of Data Centres: Some Answers and Some Questions".

[66] T. Gebrael, et al., Thermally conductive electrically insulating electronics packaging for water immersion cooling, pp. 1–1, IEEE Trans. Compon. Packag. Manuf. Technol. (2025), https://doi.org/10.1109/TCPMT.2025.3558669.

[67] T. Gebrael, A.R. Gamboa, J. LI, N. Miljkovic, and S. Aflatounian, Multilayered nonpolar, chromium, copper material coatings of power electronics boards for thermal management, US12342449B2, Jun. 24, 2025 Accessed: Jul. 04, 2025. [Online]. Available: ⟨https://patents.google.com/patent/US12342449B2/en⟩.

[68] K. Min, T. Kang, T.Y. Kang, J.-B. Pyo, Evaluation of leakage currents of semiconductor packages due to high-voltage stress under an immersion cooling environment, Appl. Sci. 15 (9) (2025) 4668, https://doi.org/10.3390/app15094668.

[69] H. Shrigondekar, Y.-C. Lin, C.-C. Wang, Investigations on performance of single-phase immersion cooling system, Int. J. Heat. Mass Transf. 206 (2023) 123961, https://doi.org/10.1016/j.ijheatmasstransfer.2023.123961.

[70] S.-M. Lee, et al., Reliability of immersion coolant and PCB materials evaluated through accelerated thermal testing, pp. 1–1, IEEE Trans. Compon. Packag. Manuf. Technol. (2025), https://doi.org/10.1109/TCPMT.2025.3594600.

[71] J.M. Shah, K. Padmanaban, H. Singh, S. Duraisamy Asokan, S. Saini, D. Agonafer, Evaluating the reliability of passive server components for single-phase immersion cooling, J. Electron. Packag (2021), https://doi.org/10.1115/1.4052536.

[72] S.W. Churchill, M. Bernstein, A correlating equation for forced convection from gases and liquids to a circular cylinder in crossflow, J. Heat. Transf. 99 (2) (1977) 300–306, https://doi.org/10.1115/1.3450685.
[73] H. Rezaei, M. Rajabi-Kochi, M. Ebrahimiazar, M. Zargartalebi, S.M. Moosavi, D. Sinton, Metric-based evaluation of electric vehicle battery immersion coolants, J. Energy Storage 140 (2025) 119036, https://doi.org/10.1016/j.est.2025.119036.
[74] X. Chen, et al., Thermal performance evaluation of electronic fluorinated liquids for single-phase immersion liquid cooling, Int. J. Heat. Mass Transf. 220 (2024) 124951, https://doi.org/10.1016/j.ijheatmasstransfer.2023.124951.
[75] A. Ruichek, et al., Immersion cooling fluid comparison using a single-phase immersion/liquid technique for data centers, Appl. Therm. Eng. 280 (2025) 128355, https://doi.org/10.1016/j.applthermaleng.2025.128355.
[76] X. Chen, et al., Thermal performance evaluation of electronic fluorinated liquids for single-phase immersion liquid cooling, Int. J. Heat. Mass Transf. 220 (2024) 124951, https://doi.org/10.1016/j.ijheatmasstransfer.2023.124951.
[77] "IPDQ60T017S7 - 500 V-950 V CoolMOSTM N-channel power MOSFET | Infineon Technologies." Accessed: Sep. 07, 2025. [Online]. Available: ⟨https://www.infineon.com/part/IPDQ60T017S7⟩.
[78] B. Kwon, T. Foulkes, T. Yang, N. Miljkovic, W.P. King, Air jet impingement cooling of electronic devices using additively manufactured nozzles, IEEE Trans. Compon. Packag. Manuf. Technol. 10 (2) (2020) 220–229, https://doi.org/10.1109/TCPMT.2019.2936852.
[79] S. Kim, R.A. Stavins, E. Shoham, G. Ziskind, N. Miljkovic, W.P. King, High power transient thermal management with dynamic phase change material and liquid cooling, Int. J. Heat. Mass Transf. 246 (2025) 126998, https://doi.org/10.1016/j.ijheatmasstransfer.2025.126998.
[80] T. Foulkes, et al., Jumping droplets electronics cooling: promise versus reality, Appl. Phys. Lett. 116 (20) (2020) 203701, https://doi.org/10.1063/5.0002537.
[81] "API 1509 Documents." Accessed: Dec. 16, 2025. [Online]. Available: ⟨https://www.api.org/products-and-services/engine-oil/documents/api-1509-documents⟩.
[82] "REF200 data sheet, product information and support | TI.com." Accessed: Aug. 05, 2025. [Online]. Available: ⟨https://www.ti.com/product/REF200⟩.
[83] G. Dou, P. Webb, D. Whalley, D. Hutt, A.R. Wilson, Current leakage failure of conformally coated electronic assemblies, Loughb. Univ. (2008), https://doi.org/10.1109/ESTC.2008.4684526%5D.
[84] U. Rathinavelu, M.S. Jellesen, P. MØller, R. Ambat, Effect of no-clean flux residues on the performance of acrylic conformal coating in aggressive environments, E E E Trans. Compon. Packag. Manuf. Technol. 2 (4) (2012) 719–728, https://doi.org/10.1109/TCPMT.2012.2186456.
[85] "Surface Insulation Resistance of Conformally Coated Printed Circuit Boards Processed With No-Clean Flux | Request PDF." Accessed: Jul. 28, 2025. [Online]. Available: ⟨https://www.researchgate.net/publication/3425155_Surface_Insulation_Resistance_of_Conformally_Coated_Printed_Circuit_Boards_Processed_With_No-Clean_Flux⟩.
[86] "OCP Base Specification for Immersion Fluids - Revision 1.0, Version 1.0, ResearchGate. Accessed: Oct. 29, 2025. [Online]. Available: ⟨https://www.researchgate.net/publication/368841323_OCP_Base_Specification_for_Immersion_Fluids_-_Revision_10_Version_10⟩.
[87] "Single Phase Immersion Cooling Fluids." Accessed: Feb. 26, 2026. [Online]. Available: ⟨https://www.fuchs.com/us/en/single-phase-immersion-cooling-fluids/⟩.
[88] "Therminol XP heat transfer fluid, Eastman. Accessed: Feb. 26, 2026. [Online]. Available: ⟨https://www.eastman.com/en/products/product-detail/71093461/therminol-xp-heat-transfer-fluid⟩.
[89] "Duratherm Products | Heat Transfer Fluids, System Cleaners & Glycols, Durathermfluids. Accessed: Feb. 26, 2026. [Online]. Available: ⟨https://durathermfluids.com/products/duratherm-g/⟩.
[90] "DIPPR | Design Institute for Physical Properties." Accessed: Feb. 26, 2026. [Online]. Available: ⟨https://www.aiche.org/dippr⟩.
[91] "Low Temp Silicone Bath Fluids, Clearco Products. Accessed: Oct. 30, 2025. [Online]. Available: ⟨https://www.clearcoproducts.com/product/psf-5cst-low-temperature-silicone-bath-fluids-for-purchase/⟩.
[92] "Galden® PFPE." Accessed: Oct. 30, 2025. [Online]. Available: ⟨https://www.syensqo.com/en/brands/galden-pfpe⟩.